

Nodally integrated thermomechanical RKPM: Part II — Generalized thermoelasticity and hyperbolic finite-strain thermoplasticity

Michael Hillman^{*†} and Kuan-Chung Lin[‡]

This is a post-peer-review, pre-copyedit version of an article [to be] published in Computational Mechanics. The final authenticated version is [will be] available online at: <http://dx.doi.org/10.1007/s00466-021-02048-8>.

Abstract

In this two-part paper, a stable and efficient nodally-integrated reproducing kernel particle method (RKPM) approach for solving the governing equations of generalized thermomechanical theories is developed. Part I investigated quadrature in the weak form using classical thermoelasticity as a model problem, and a stabilized and corrected nodal integration was proposed. In this sequel, these methods are developed for generalized thermoelasticity and generalized finite-strain plasticity theories of the hyperbolic type, which are more amenable to explicit time integration than the classical theories. Generalized thermomechanical models yield finite propagation of temperature, with a so-called second sound speed. Since this speed is not well characterized for common engineering materials and environments, equating the elastic wave speed with the second sound speed is investigated to obtain results close to classical thermoelasticity, which also yields a uniform critical time step. Implementation of the proposed nodally integrated RKPM for explicit analysis of finite-strain thermoplasticity is also described in detail. Several benchmark problems are solved to demonstrate the effectiveness of the proposed approach for thermomechanical analysis.

keywords Meshfree methods, generalized thermoelasticity, thermoplasticity, nodal integration, coupled problems

1 Introduction

Part I of this paper began with investigating nodal quadrature of the Galerkin weak form in meshfree methods for thermoelasticity. It was shown that severe oscillations, orders of magnitude greater than the solution itself, were present when nodal integration was employed. This is in contrast to pure elasticity where oscillations are typically smaller than the magnitude of the true solution. This instability was also shown to be explosive in nature, yielding meaningless results for nodal integration. A naturally stabilized nodal integration (NSNI) [27] was then proposed which was

^{*}Kimball Assistant Professor, Department of Civil and Environmental Engineering, The Pennsylvania State University, University Park, PA 16802, USA.

[†]Corresponding author; email: mhillman@psu.edu; postal address: 224A Sackett Building, The Pennsylvania State University, University Park, PA 16802, USA.

[‡]Assistant Professor, Department of Civil Engineering, National Cheng Kung University, Tainan 70101, Taiwan, ROC.

shown to be effective at precluding this instability. In particular, this method provides a highly efficient solution without tunable parameters typical of stabilization approaches. The n th order variational consistency conditions were then derived for the two-field problem, and an efficient correction was proposed resulting in a variationally consistent naturally stabilized nodal integration (VC-NSNI). Importantly, as shown in [55], satisfaction of the variational consistency conditions is necessary to ensure convergence of the numerical solution, whereas traditional approaches cannot meet these conditions.

This next part focuses on the development of this stabilized and corrected nodal quadrature in RKPM for generalized thermoelasticity, and generalized finite-strain thermoplasticity. Particular emphasis is given to explicit analysis.

As discussed in Part I, the need for solving partially- or fully-coupled systems may arise due to many physical phenomena. Sub-classes of these problems also involve a large degree of material deformation, flow, and failure. Here, the traditional mesh-based methods suffer from mesh-distortion under large deformations, and are ineffective in dealing with material failure and associated topological changes in the domain present in related applications such as additive (e.g. 3-D printing — topological changes) and subtractive (e.g., machining — both) manufacturing techniques where coupling between the displacement and temperature can be present. Meshfree methods such as RKPM on the other hand, which are point-based and do not require a mesh, are quite adept at handling these phenomena [11, 13].

In Part I, the *classical* thermoelasticity theory [22] was discussed. While the equation of motion is a hyperbolic equation, the energy equation is parabolic. This provides a finite propagation speed for displacements but an infinite propagation speed for the temperature, which is non-physical: for instance, this violates the theory of special relativity by propagating information faster than light. As an alternative to the classical equations, generalized thermoelasticity theories [39, 24] have been developed, in which the energy equation is of the hyperbolic type. These theories are referred to as thermoelasticity with a so-called *second sound*. Part I of this work dealt with the classical theory; Part II will deal with these generalized theories, as well as finite-strain plasticity of the parabolic and hyperbolic types [9, 52, 20]. The numerical motivation for the use of these theories is of course, to provide efficient explicit analysis, where the time step is directly proportional to the nodal spacing rather than its square.

There are several generalized thermoelasticity theories. One popular theory is the Lord and Shulman (L-S) theory [39], based on a modified Fourier Law of heat conduction using a relaxation time. Another well-established generalized thermoelasticity theory is the Green and Lindsay (G-L) theory [24] based on an entropy production inequality. This theory uses two relaxation times, in the Duhamel-Neumann law and the entropy density. In both theories, the energy equation becomes hyperbolic, and thus the temperature propagation has a finite velocity.

Numerical solutions based on the L-S theory have been reported using FEM [44]. BEM [10, 51] also provides good results in thermoelastic problems using both the G-L theory and L-S theory. Thermoelasticity theories with a second sound have been studied in various problems, such as a layer of isotropic homogeneous material [5],

thermal shock problems with a crack [47, 40, 58, 1, 48, 30], and rotating disks [33].

For finite strain thermoplasticity, FEM methods have been developed for simulating large deformation problems, such as necking processes [50, 3, 56, 7], modelling of welding [37], ballistic penetration of metallic targets [8], and orthogonal high-speed machining [41]. Other mesh-based methods also have been used to simulate the necking process, for example, the mixed finite element method [50] and the updated enhanced assumed strain finite element formalism [2]. Of course, these finite element-based methods suffer from mesh distortion issues under large deformations, and are ineffective at dealing with material flow and separation [36, 11].

Recently, meshfree approximations have been used to study the generalized thermoelasticity theories. Various methods have been used, for example, the Meshless local Petrov–Galerkin method [29] as well as methods using radial basis functions [57]. Meshfree methods have also been developed for finite-strain thermoplasticity. Simulations have included ductile fracture [49] and friction drilling [43, 54]. Based on variational thermomechanical constitutive updates and the optimal transportation meshfree (OTM) method [34], the hot OTM method (HOTM) [53] has been developed for modeling external heating and cooling behavior. The HOTM method has mostly been applied to laser cladding technology [23]. Yet, virtually none of these meshfree approaches to thermomechanical equations discussed consider any advanced domain integration techniques other than [43, 54], regardless of the use of classical or generalized equations. For a review of existing techniques and an in-depth discussion on meshfree quadrature including [43, 54], see Part I of this paper.

In this work, the methods developed in the prequel are developed for generalized thermoelasticity, and generalized thermoplasticity. Namely, the variationally consistent naturally stabilized nodal integration (VC-NSNI) technique is extended to both of these problems. For generalized thermoelasticity, the extension of these two methods is straightforward. Strains and temperature gradients are expanded with implicit gradient approximations for stabilization as before, and the correction remains the same. In finite-strain thermoplasticity, the Cauchy stress and associated variation on strain are instead expanded to stabilize the results. Finally, since the propagation speed of temperature is not well-characterized for most engineering materials, and in most settings (typically this is reported near absolute zero for special materials such as superfluids), equating the second sound speed to the first is investigated. This yields a critical time step in explicit analysis that is the same as in pure solid mechanics problems, but meanwhile very small relaxation times such that the solution is close to the classical theory, which is widely accepted as a good model for thermomechanical problems.

The remainder of this paper is organized as follows. The general governing equations of the coupled thermomechanical theory are discussed in Section 2. In Section 3 classical and generalized thermoelasticity are introduced as special cases, with the RKPM discretization of the weak form given. Section 4 develops thermoplasticity as another more general case, with the Lagrangian RKPM discretization given along with associated explicit algorithms. In Section 5 the time-step criteria is discussed. Benchmarks are then solved for generalized thermoelasticity and classical and generalized thermoplasticity in Section 6, where equating the first and second sound speed

is also investigated. Final concluding remarks for this two-part paper are given in Section 7.

2 Governing equations of the coupled thermal-mechanical theory

In this section, we review the general governing equations for all of the aforementioned thermomechanical theories. Ultimately, they consist of the balance of energy, and the balance of momentum. The subsequent assumptions used in these equations yield both thermoelasticity and thermoplasticity.

2.1 Dissipation inequality and balance of energy

For the thermomechanical problem, the dissipation inequality can be written as

$$\frac{1}{\rho} \boldsymbol{\sigma} : \dot{\boldsymbol{\varepsilon}} - \dot{e} + \theta \eta - \frac{1}{\rho \theta} \mathbf{q} \cdot \nabla \theta \geq 0 \quad (1)$$

where $(\dot{\quad})$ denotes a material time rate of change (herein $(\ddot{\quad})$ will denote the second-order material time derivative; all terms are Lagrangian), ρ is the density, $\boldsymbol{\sigma}$ is the Cauchy stress, $\dot{\boldsymbol{\varepsilon}}$ is the rate of deformation, \dot{e} is the time rate of change of the internal energy, $\theta \equiv T - T_0$ is the temperature change and herein is treated as a primary unknown; T is the absolute temperature, T_0 is the reference temperature, η is the entropy, and \mathbf{q} the heat flux.

Equation (1) can be decomposed into the conductive thermal Ω_{con} , and thermo-mechanical Ω_{thermech} , parts as:

$$\Omega_{\text{thermech}} = \frac{1}{\rho} \boldsymbol{\sigma} : \dot{\boldsymbol{\varepsilon}} - \dot{e} + \theta \eta \geq 0 \quad (2a)$$

$$\Omega_{\text{con}} = - \frac{1}{\rho \theta} \mathbf{q} \cdot \nabla \theta \geq 0. \quad (2b)$$

From the fact that the density ρ and the absolute temperature change θ are always positive, using (2b) one can deduce that

$$\mathbf{q} \cdot \nabla \theta \leq 0. \quad (3)$$

This is Fourier's inequality which states that heat flows from a hot region to a cold region. This can be assured by Duhamel's law of heat conduction

$$\mathbf{q} = -\mathbf{k}(\mathbf{F}, \theta) \cdot \nabla \theta \quad (4)$$

where \mathbf{F} is the deformation gradient and the thermal conductivity tensor \mathbf{k} is positive-definite. Assuming an isotropic material, one obtains Fourier's law of heat conduction $\mathbf{k} = \mathbf{I}k$ with isotropic scalar conductivity k .

Next, we introduce the balance of energy

$$\rho \dot{e} + \nabla \cdot \mathbf{q} = \boldsymbol{\sigma} : \dot{\boldsymbol{\varepsilon}} + Q \quad (5)$$

where Q is the heat source, and here we assume the Helmholtz free energy ϕ contains elastic and plastic entropy [50]:

$$\phi \equiv e - \theta(\eta - \eta^p) \quad (6)$$

where η , η^p , and $\eta^e = \eta - \eta^p$ are the total entropy, the plastic entropy, and the elastic entropy, respectively.

Substitution (5) and (6) into (2a) yields

$$\nabla \cdot \mathbf{q} + \theta\dot{\eta} = Q. \quad (7)$$

This is the balance of energy for both thermoelasticity and thermal plasticity.

2.2 Governing equations of the coupled thermal-mechanical theory

The balance of energy in the current configuration $\Omega^{\mathbf{x}}$ with boundary $\Gamma^{\mathbf{x}}$ over time interval $]0, t_f[$ can thus be obtained as

$$\nabla_{\mathbf{x}} \cdot \mathbf{q} + \theta\dot{\eta} = Q \quad \text{on } \Omega^{\mathbf{x}} \times]0, t_f[\quad (8)$$

where $\nabla_{\mathbf{x}}$ is the Del operator associated with current configuration with coordinates \mathbf{x} . For small-strain linear elastic problems, $\nabla_{\mathbf{x}}$ is simply Del and there is no distinction between the current configuration and the reference configuration, and in this case we denote the domain as Ω .

The conservation of momentum in the current configuration can be expressed as:

$$\rho\ddot{\mathbf{u}} = \nabla_{\mathbf{x}} \cdot \boldsymbol{\sigma} + \mathbf{b} \quad \text{on } \Omega^{\mathbf{x}} \times]0, t_f[\quad (9)$$

where $\ddot{\mathbf{u}} \equiv \partial^2 \mathbf{u} / \partial t^2$ is the acceleration; \mathbf{u} is the displacement field and herein is treated as a primary unknown, $\boldsymbol{\sigma}$ is the Cauchy stress tensor, and \mathbf{b} is the prescribed body force. Again for small-strain linear elastic problems, in the above $\nabla_{\mathbf{x}} = \nabla$ and $\Omega^{\mathbf{x}} = \Omega$.

The boundary conditions in the current configuration are:

$$\mathbf{u} = \mathbf{g} \quad \text{on } \Gamma_{\mathbf{g}}^{\mathbf{x}} \times]0, t_f[\quad (10a)$$

$$\boldsymbol{\sigma} \cdot \mathbf{n} = \mathbf{h} \quad \text{on } \Gamma_{\mathbf{h}}^{\mathbf{x}} \times]0, t_f[\quad (10b)$$

$$\theta = \bar{\theta} \quad \text{on } \Gamma_T^{\mathbf{x}} \times]0, t_f[\quad (10c)$$

$$\mathbf{n} \cdot \mathbf{q} = \bar{q} \quad \text{on } \Gamma_q^{\mathbf{x}} \times]0, t_f[\quad (10d)$$

where \mathbf{g} , \mathbf{n} , \mathbf{h} , $\bar{\theta}$, \bar{q} denote prescribed displacement, outward unit normal to the surface, prescribed traction, prescribed temperature difference, and prescribed heat flux, respectively, with $\overline{\Gamma_{\mathbf{g}}^{\mathbf{x}} \cup \Gamma_{\mathbf{h}}^{\mathbf{x}}} = \overline{\Gamma_T^{\mathbf{x}} \cup \Gamma_q^{\mathbf{x}}} = \Gamma$ and $\Gamma_{\mathbf{g}}^{\mathbf{x}} \cap \Gamma_{\mathbf{h}}^{\mathbf{x}} = \Gamma_T^{\mathbf{x}} \cap \Gamma_q^{\mathbf{x}} = \emptyset$. For small-strain linear thermoelastic problems, we drop the super-scripts on the boundary terms as there is no distinction between the boundary of the reference configuration and current configuration.

To complete the problem, the constitutive laws for \mathbf{q} and $\boldsymbol{\sigma}$ need to be specified. In turn, these dictate the nature of the coupling between the displacement \mathbf{u} and temperature change θ .

3 Generalized thermoelasticity

Assuming the free energy function $\phi(\boldsymbol{\varepsilon}, \theta)$ and the entropy $\eta^e(\boldsymbol{\varepsilon}, \theta)$ for small strain thermoelasticity, the following equations are obtained (see appendix A for assumptions) for thermoelasticity over the domain Ω and time interval $]0, t_f[$:

$$\nabla \cdot \boldsymbol{\sigma} + \mathbf{b} = \rho \ddot{\mathbf{u}} \quad (11)$$

$$-\nabla \cdot \mathbf{q} - \rho c_p \dot{\theta} + Q - \beta T_0 \nabla \cdot \dot{\mathbf{u}} = 0 \quad (12)$$

where c_p is the specific heat capacity, and $\beta = \alpha(3\lambda + 2\mu)$ is the thermal stress modulus; α is the thermal expansion coefficient, λ and μ are Lamé's first and second constants.

3.1 Classical thermoelasticity

To outline the differences in the generalized and classical thermoelastic theories, here we review the basic assumptions in isotropic thermoelasticity. For the constitutive laws, the heat flux in (4) takes the form

$$\mathbf{q} = -k \nabla \theta \quad (13)$$

which is the Fourier law. For the stress, the Duhamel-Neumann law is adopted:

$$\boldsymbol{\sigma} = \mathbb{C} : \boldsymbol{\varepsilon} - \beta \theta \mathbb{I} \quad (14)$$

where \mathbb{C} and $\boldsymbol{\varepsilon}$ are the isotropic fourth-order elastic tensor, and infinitesimal strain tensor, respectively, and \mathbb{I} is the second-order identity tensor. Employing (14) in the momentum equation (11) and the Fourier law (13) in the energy equation (12), the classical equations of thermoelasticity employed in Part I of this paper are obtained.

3.2 Lord and Shulman's theory

Lord and Shulman (denoted as L-S) introduced a relaxation time t_0 in the classical Fourier law (13) of heat conduction as follows [39]:

$$\mathbf{q} + t_0 \dot{\mathbf{q}} = -k \nabla \theta. \quad (15)$$

The classical Duhamel-Neumann law (14) is still considered. Employing (14) in (11) and the modified Fourier diffusion law (15) in the energy equation (12), the following governing equations of the Lord and Shulman theory can be written as

$$\nabla \cdot (\mathbb{C} : \boldsymbol{\varepsilon}(\mathbf{u}) - \beta \theta \mathbb{I}) + \mathbf{b} = \rho \ddot{\mathbf{u}}, \quad (16a)$$

$$-t_0 \rho c_p \ddot{\theta} - t_0 \beta T_0 \nabla \cdot \ddot{\mathbf{u}} + \nabla \cdot k \nabla \theta - \rho c_p \dot{\theta} + (Q + t_0 \dot{Q}) - \beta T_0 \nabla \cdot \dot{\mathbf{u}} = 0. \quad (16b)$$

If $t_0 = 0$, then classical isotropic thermoelasticity is recovered.

The corresponding finite temperature propagation speed of L-S theory, $c_{T,LS}$, can be obtained as

$$c_{T,LS} = \sqrt{\frac{k}{t_0 \rho c_p}}. \quad (17)$$

3.3 Green and Lindsay's theory

Based on an entropy production inequality, Green and Lindsay's theory (denoted as G-L) considers two relaxation times [24].

The first relaxation time t_1 enters into the Duhamel-Neumann law (14):

$$\boldsymbol{\sigma} = \mathbb{C} : \boldsymbol{\varepsilon}(\mathbf{u}) - \beta(\theta + t_1\dot{\theta})\mathbb{I}. \quad (18)$$

A second relaxation time t_2 is considered in the following entropy density function:

$$\eta = \eta_0 + \frac{c_p}{T_0}\theta + \frac{c_p t_2}{T_0}\dot{\theta} + \frac{1}{\rho}\beta\nabla \cdot \mathbf{u} \quad (19)$$

where η_0 is the reference entropy density.

The Duhamel-Neumann law with relaxation time (18) and the entropy density function (19) are introduced in the equation of motion (11) and in the energy equation (12) to yield:

$$\nabla \cdot (\mathbb{C} : \boldsymbol{\varepsilon}(\mathbf{u}) - \beta(\theta + t_1\dot{\theta})\mathbb{I}) + \mathbf{b} = \rho\ddot{\mathbf{u}}, \quad (20a)$$

$$-t_2\rho c_p\ddot{\theta} + \nabla \cdot k\nabla\theta - \rho c_p\dot{\theta} + Q - \beta T_0\nabla \cdot \dot{\mathbf{u}} = 0. \quad (20b)$$

Note that if $t_1 = t_2 = 0$, then the classical governing equations are recovered.

The corresponding temperature propagation speed in the G-L theory, $c_{T,GL}$, is given as

$$c_{T,GL} = \sqrt{\frac{k}{t_2\rho c_p}}. \quad (21)$$

3.4 Unified generalized thermoelasticity

For convenience, the classical, G-L, and L-S theories can be expressed as a generalized thermoelasticity formulation as follows:

$$\nabla \cdot (\mathbb{C} : \boldsymbol{\varepsilon}(\mathbf{u}) - \beta(\theta + t_1\dot{\theta})\mathbb{I}) + \mathbf{b} = \rho\ddot{\mathbf{u}}, \quad (22a)$$

$$-(t_0 + t_2)\rho c_p\ddot{\theta} - t_0\beta T_0\nabla \cdot \dot{\mathbf{u}} + \nabla \cdot k\nabla\theta - \rho c_p\dot{\theta} + (Q + t_0\dot{Q}) - \beta T_0\nabla \cdot \dot{\mathbf{u}} = 0. \quad (22b)$$

In the above, when all relaxation times are zero ($t_0 = t_1 = t_2 = 0$), classical thermoelasticity is recovered. The G-L theory can be obtained with $t_0 = 0$, and the L-S theory can be obtained by setting $t_1 = t_2 = 0$. In following sections, the governing equations for generalized thermoelasticity (22) are employed to make the derivations concise.

Now, to distinguish between a fully coupled and a partially coupled problem, the following thermoelasticity coupling parameter is introduced for convenience:

$$\delta = \frac{\beta^2 T_0}{\rho c(\lambda + 2\mu)}. \quad (23)$$

When $\delta = 0$ the system is the uncoupled (or partially coupled). On the other hand, if δ is non-zero value, it is the fully coupled case. In practice, one may select the former case when $\delta \approx 0$. It can be noted that this depends on the ratio of material constants at hand, and may differ for e.g., many metals $\delta \approx 0$, and several composites and plastics $\delta \gg 1$.

3.5 Weak form of generalized thermoelasticity

RKPM employs the weak forms of the governing equations. Using the weighted residual method, applying integration-by-parts and the divergence theorem, the weak forms can be derived as: find $\mathbf{u} \in U_g$, $U_g = \{\mathbf{u} \mid \mathbf{u} \in H^1, \mathbf{u} = \mathbf{g} \text{ on } \Gamma_g \times]0, t_f[\}$ and $\theta \in \Theta_T$, $\Theta_T = \{\theta \mid \theta \in H^1, \theta = \bar{\theta} \text{ on } \Gamma_T \times]0, t_f[\}$ such that for all $\mathbf{v} \in U_0$, $U_0 = \{\mathbf{v} \mid \mathbf{v} \in H^1, \mathbf{v} = \mathbf{0} \text{ on } \Gamma_g \times]0, t_f[\}$ and $S \in \Theta_0$, $\Theta_0 = \{S \mid S \in H^1, S = 0 \text{ on } \Gamma_T \times]0, t_f[\}$ the following equations hold:

$$\begin{aligned} & \int_{\Omega} \rho \mathbf{v} \cdot \dot{\mathbf{u}} d\Omega + \int_{\Omega} \nabla^s \mathbf{v} : \mathbb{C} : \nabla^s \mathbf{u} d\Omega - \int_{\Omega} \beta \nabla \cdot \mathbf{v} (\theta + t_1 \dot{\theta}) d\Omega = \\ & \int_{\Omega} \mathbf{v} \cdot \mathbf{b} d\Omega + \int_{\Gamma_h} \mathbf{v} \cdot \mathbf{h} d\Gamma, \quad (24a) \\ & - \int_{\Omega} (t_0 + t_2) \rho c_p S \ddot{\theta} d\Omega - \int_{\Omega} t_0 \beta T_0 S \nabla \cdot \dot{\mathbf{u}} d\Omega + \int_{\Omega} k \nabla S \cdot \nabla \theta d\Omega + \int_{\Omega} \rho c_p S \dot{\theta} d\Omega - \\ & \int_{\Omega} \beta T_0 S \nabla \cdot \dot{\mathbf{u}} d\Omega = \int_{\Omega} S (Q + t_0 \dot{Q}) d\Omega + \int_{\Gamma_q} S \bar{q} d\Gamma, \quad (24b) \end{aligned}$$

where ∇^s denotes the symmetric part of the gradient.

As noted in Part I, both "energy" terms contain gradients of the primary unknown, $\nabla \theta$ and $\nabla \mathbf{u}$, in (24a) and (24b), respectively. Thus, when discretized by meshfree shape functions, it is easy to show that an oscillatory mode with a wavelength of twice the nodal spacing, in both displacement and temperature, will not contribute to these terms when away from the influence of the boundary, and this mode can potentially grow virtually unrestricted [27]. In Part I, it was further demonstrated that in thermoelasticity, these modes do in fact grow unrestricted, and are explosive in nature yielding meaningless results without a stabilized nodal integration. It was also shown that these oscillations were many orders of magnitude worse than pure elasticity.

3.6 Galerkin form

The Galerkin approximation of (24) asks to find $\mathbf{u}^h \in U^h \subset U_g^1$ and $\theta^h \in \Theta_T^h \subset \Theta_T^1$, such that for all $\mathbf{v}^h \in V^h \subset U_0^1$ and $S^h \in \Theta_0^h \subset \Theta_0^1$ the following equations hold:

$$\begin{aligned} & \int_{\Omega} \rho \mathbf{v}^h \cdot \dot{\mathbf{u}}^h d\Omega + \int_{\Omega} \nabla^s \mathbf{v}^h : \mathbb{C} : \nabla^s \mathbf{u}^h d\Omega - \int_{\Omega} \beta \nabla \cdot \mathbf{v}^h (\theta^h + t_1 \dot{\theta}^h) d\Omega = \\ & \int_{\Omega} \mathbf{v}^h \cdot \mathbf{b} d\Omega + \int_{\Gamma_h} \mathbf{v}^h \cdot \mathbf{h} d\Gamma, \quad (25a) \end{aligned}$$

$$\begin{aligned} & - \int_{\Omega} (t_0 + t_2) \rho c_p S^h \ddot{\theta}^h d\Omega - \int_{\Omega} t_0 \beta T_0 S^h \nabla \cdot \dot{\mathbf{u}}^h d\Omega + \int_{\Omega} k \nabla S^h \cdot \nabla \theta^h d\Omega + \\ & \int_{\Omega} \rho c_p S^h \dot{\theta}^h d\Omega - \int_{\Omega} \beta T_0 S^h \nabla \cdot \dot{\mathbf{u}}^h d\Omega = \int_{\Omega} S^h (Q + t_0 \dot{Q}) d\Omega + \int_{\Gamma_q} S^h \bar{q} d\Gamma. \quad (25b) \end{aligned}$$

3.7 Reproducing kernel approximation

In this section, the reproducing kernel (RK) approximation for the linear problem is briefly reviewed, along with its implicit gradient counterpart used in the stabilization. For more details, see Part I.

Let a domain $\bar{\Omega} = \Omega \cup \Gamma$ be discretized by a set of NP nodes $\mathcal{S} = \{\mathbf{x}_I | \mathbf{x}_I \in \bar{\Omega}\}_{I=1}^{NP}$ with associated set of node numbers $\mathcal{N} = \{I | \mathbf{x}_I \in \mathcal{S}\}$. The n th order reproducing kernel (RK) approximation $u^h(\mathbf{x})$ of a function $u(\mathbf{x})$ is

$$u^h(\mathbf{x}) = \sum_{I \in \mathcal{N}} \Psi_I(\mathbf{x}) u_I \quad (26)$$

where $\{\Psi_I(\mathbf{x})\}_{I \in \mathcal{N}}$ is the set of RK shape functions, and $\{u_I\}_{I \in \mathcal{N}}$ are the associated coefficients. The shape functions are composed of a kernel function $\Phi_a(\mathbf{x} - \mathbf{x}_I)$ with normalized support a and a correction function [38, 15]:

$$\Psi_I(\mathbf{x}) = \mathbf{H}(\mathbf{0})^\top \mathbf{M}(\mathbf{x})^{-1} \mathbf{H}(\mathbf{x} - \mathbf{x}_I) \Phi_a(\mathbf{x} - \mathbf{x}_I). \quad (27)$$

where $\mathbf{H}(\mathbf{0})^\top \mathbf{M}(\mathbf{x})^{-1} \mathbf{H}(\mathbf{x} - \mathbf{x}_I)$ is the correction function; \mathbf{H} is a column vector of complete n th order monomials, and \mathbf{M} is the moment matrix defined as follows:

$$\mathbf{M}(\mathbf{x}) = \sum_{I \in \mathcal{N}} \mathbf{H}(\mathbf{x} - \mathbf{x}_I) \mathbf{H}(\mathbf{x} - \mathbf{x}_I)^\top \Phi_a(\mathbf{x} - \mathbf{x}_I). \quad (28)$$

Due to the correction function, the RK approximation can be shown to satisfy the following reproducing conditions:

$$\sum_{I \in \mathcal{N}} \Psi_I(\mathbf{x}) \mathbf{H}(\mathbf{x}_I) = \mathbf{H}(\mathbf{x}) \quad (29)$$

Note that because of the product rule, taking direct derivatives of (27) becomes increasingly expensive as the order of differentiation increases. In NSNI, the gradients of gradients are necessary due to the Taylor series expansion involved. Thus, the following implicit gradient approximation to a gradient term $u(\mathbf{x})_{,i} \equiv \partial u / \partial x_i$ is introduced to alleviate the computational burden [19, 35]:

$$u(\mathbf{x})_{,i} \approx \sum_{I \in \mathcal{N}} \Psi_{Ii}^\nabla(\mathbf{x}) u_I \quad (30)$$

where Ψ_{Ii}^∇ is the implicit gradient shape function which takes the form:

$$\Psi_{Ii}^\nabla(\mathbf{x}) = [\mathbf{H}_i^\nabla]^\top \mathbf{M}(\mathbf{x})^{-1} \mathbf{H}(\mathbf{x} - \mathbf{x}_I) \Phi_a(\mathbf{x} - \mathbf{x}_I) \quad (31)$$

where \mathbf{M} is the same moment matrix in (28), and \mathbf{H}_i^∇ is a column vector of the form:

$$\mathbf{H}_i^\nabla = [0, \dots, 0, -1, 0, \dots, 0]^\top \quad (32)$$

where -1 is $(i+1)^{th}$ entry. Similar to the RK approximation (27), here $[\mathbf{H}_i^\nabla]^\top \mathbf{M}(\mathbf{x})^{-1} \mathbf{H}(\mathbf{x} - \mathbf{x}_I)$ is a correction function. It can be shown that due to this correction, the implicit gradient approximation satisfies the following gradient reproducing conditions:

$$\sum_{I \in \mathcal{N}} \Psi_{Ii}^\nabla(\mathbf{x}) \mathbf{H}(\mathbf{x}_I) = \mathbf{H}(\mathbf{x})_{,i}. \quad (33)$$

Comparing (29) to (33), it can be seen that the implicit gradient possesses the same key properties in gradient approximations, while much less computationally demanding. For more details, consult Part I, or see [11].

3.8 Matrix forms

Naturally stabilized nodal integration, and variationally consistent integration introduced in Part I are both straightforwardly applied to the present generalized thermoelastic problem. The natural stabilization follows the exact same derivation and formulation, since no new terms are introduced into the bilinear forms of the generalized formulation (24).

Similarly, the present formulation only introduced additional time-dependent terms. Meanwhile, the variational consistency conditions are based on the steady problem. Therefore it is easy to show that the variational consistency conditions for the generalized formulation remain the same, and the test function gradient correction from Part I thus also remains the same. That is, the integration constraints, and associated correction for (25) are identical. We refer the interested reader to Part I of this paper for the details of test and trial function construction, and related corrections and stabilization.

Proceeding to introduce the RK approximation (26) with associated NSNI stabilization and VC correction from Part I into the nodally-integrated Galerkin equation (25), one obtains the following matrix form:

$$\begin{bmatrix} \mathbf{M}_{uu} & \mathbf{0} \\ \mathbf{M}_{\theta u} & \mathbf{M}_{\theta\theta} \end{bmatrix} \begin{bmatrix} \ddot{\mathbf{u}} \\ \ddot{\boldsymbol{\theta}} \end{bmatrix} + \begin{bmatrix} \mathbf{0} & \mathbf{C}_{u\theta} \\ \mathbf{C}_{\theta u} & \mathbf{C}_{\theta\theta} \end{bmatrix} \begin{Bmatrix} \dot{\mathbf{u}} \\ \dot{\boldsymbol{\theta}} \end{Bmatrix} + \begin{bmatrix} \mathbf{K}_{uu} & \mathbf{K}_{u\theta} \\ \mathbf{0} & \mathbf{K}_{\theta\theta} \end{bmatrix} \begin{Bmatrix} \mathbf{u} \\ \boldsymbol{\theta} \end{Bmatrix} = \begin{Bmatrix} \mathbf{F}^{ext} \\ \mathbf{Q}^{ext} \end{Bmatrix} \quad (34)$$

where \mathbf{u} and $\boldsymbol{\theta}$ are the row vectors of the unknowns $\{\mathbf{u}_I\}_{I=1}^{NP}$ and $\{\boldsymbol{\theta}_I\}_{I=1}^{NP}$, respectively,

and for a homogeneous media in two dimensions:

$$\mathbf{M}_{uu} = \sum_{L=1}^{NP} \rho \mathbf{N}(\mathbf{x}_L)^\top \mathbf{N}(\mathbf{x}_L) W_L \quad (35a)$$

$$\mathbf{M}_{\theta u} = \sum_{L=1}^{NP} -t_0 T_0 \beta \Psi(\mathbf{x}_L)^\top \mathbf{I} \mathbf{B}^u(\mathbf{x}_L) W_L \quad (35b)$$

$$\mathbf{M}_{\theta\theta} = \sum_{L=1}^{NP} -\rho c_p (t_0 + t_2) \Psi(\mathbf{x}_L)^\top \Psi(\mathbf{x}_L) W_L \quad (35c)$$

$$\mathbf{C}_{u\theta} = \sum_{L=1}^{NP} -t_1 \beta \Psi(\mathbf{x}_L)^\top \mathbf{B}^\theta(\mathbf{x}_L) W_L \quad (35d)$$

$$\mathbf{C}_{\theta u} = -T_0 \mathbf{K}_{u\theta}^\top \quad (35e)$$

$$\mathbf{C}_{\theta\theta} = \sum_{L=1}^{NP} \rho c_p \Psi(\mathbf{x}_L)^\top \Psi(\mathbf{x}_L) W_L \quad (35f)$$

$$\mathbf{K}_{uu} = \sum_{L=1}^{NP} (\mathbf{B}^{uc}(\mathbf{x}_L))^\top \mathbf{D} \mathbf{B}^u(\mathbf{x}_L) W_L + \sum_{L=1}^{NP} \sum_{i=1}^2 (\mathbf{B}_i^{u\nabla}(\mathbf{x}_L))^\top \mathbf{D} \mathbf{B}_i^{u\nabla}(\mathbf{x}_L) M_{Li} \quad (35g)$$

$$\mathbf{K}_{u\theta} = - \sum_{L=1}^{NP} \beta (\mathbf{B}^{uc}(\mathbf{x}_L))^\top \mathbf{I} \Psi(\mathbf{x}_L) W_L \quad (35h)$$

$$\mathbf{K}_{\theta\theta} = \sum_{L=1}^{NP} k (\mathbf{B}^{\theta c}(\mathbf{x}_L))^\top \mathbf{B}^\theta(\mathbf{x}_L) W_L + \sum_{L=1}^{NP} \sum_{i=1}^2 k (\mathbf{B}_i^{\theta\nabla}(\mathbf{x}_L))^\top \mathbf{B}_i^{\theta\nabla}(\mathbf{x}_L) M_{Li} \quad (35i)$$

$$\mathbf{F}^{\text{ext}} = \sum_{L=1}^{NP} \mathbf{N}(\mathbf{x}_L)^\top \mathbf{b} W_L + \sum_{K=1}^{NBPu} \mathbf{N}(\mathbf{x}_K)^\top \mathbf{h} L_K^u \quad (35j)$$

$$\mathbf{Q}^{\text{ext}} = \sum_{L=1}^{NP} \Psi(\mathbf{x}_L)^\top Q W_L + \sum_{K=1}^{NBP\theta} \Psi(\mathbf{x}_K)^\top \bar{q} L_K^\theta \quad (35k)$$

where $\mathbf{I} = [1 \ 1 \ 0 \ 0]^\top$, \mathbf{D} is the matrix corresponding to the tensor \mathbb{C} , W_L is the integration weight of node L , and L_K^u and L_K^θ denote the K th weight of one of the $NBPu$ and $NBP\theta$ integration points on the natural boundary, respectively. The definition of the terms \mathbf{N} , Ψ , \mathbf{B}^u , \mathbf{B}^θ , \mathbf{B}^{uc} , $\mathbf{B}^{\theta c}$, $\mathbf{B}_i^{u\nabla}$, and $\mathbf{B}_i^{\theta\nabla}$ can be found in Part I.

Compared to classical thermoelasticity, there are three additional terms in (35b), (35c), and (35d), which emanate from the relaxation times introduced. Therefore the generalized formulation can easily be introduced into existing classical thermoelasticity codes, provided time integration is taken care of.

The final semi-discrete linear time-dependent system (34) can be written in compact form as

$$\mathbf{M}\ddot{\mathbf{d}}(t) + \mathbf{C}\dot{\mathbf{d}}(t) + \mathbf{K}\mathbf{d}(t) = \mathbf{F}(t) \quad (36)$$

where

$$\mathbf{M} = \begin{bmatrix} \mathbf{M}_{uu} & \mathbf{0} \\ \mathbf{M}_{\theta u} & \mathbf{M}_{\theta\theta} \end{bmatrix}, \quad \mathbf{C} = \begin{bmatrix} \mathbf{0} & \mathbf{C}_{u\theta} \\ \mathbf{C}_{\theta u} & \mathbf{C}_{\theta\theta} \end{bmatrix}, \quad \mathbf{K} = \begin{bmatrix} \mathbf{K}_{uu} & \mathbf{K}_{u\theta} \\ \mathbf{0} & \mathbf{K}_{\theta\theta} \end{bmatrix} \quad (37)$$

and

$$\mathbf{d} = \begin{bmatrix} \mathbf{u} \\ \boldsymbol{\theta} \end{bmatrix}, \quad \mathbf{F} = \begin{bmatrix} \mathbf{F}^{\text{ext}} \\ \mathbf{Q}^{\text{ext}} \end{bmatrix}. \quad (38)$$

In this work, time integration is carried out using the Newmark method [31]. For the explicit version (central difference), since there are off-diagonal terms in the mass-type and damping-type matrices in (37), one can lump the mass and replace the velocity approximation terms with their predictors. In the numerical examples, it is shown that this has little effect on accuracy. The specific algorithms are omitted here due to their relative simplicity in the elastic case.

Later, it will be shown that the relaxation times in the generalized theories can be chosen such that critical time step for explicit time integration is the same as pure small-strain linear elasticity, thus avoiding the parabolic $\mathcal{O}(\Delta t^2)$ time step restriction, also resulting in solutions close to the classical theory.

4 Thermoplasticity

4.1 Finite-strain formulation

A non-linear analysis generally involves either the total Lagrangian or the updated Lagrangian formulation [6]. In the total Lagrangian description, strain and stress measures are defined with respect to the undeformed or reference geometry. As opposed to the total Lagrangian description, an updated Lagrangian analysis uses the current configuration. In this work, the updated Lagrangian scheme will be employed since it is applicable to extreme deformation problems where meshfree methods are adept.

Consider a body initially occupying a region $\Omega^{\mathbf{X}}$ with boundary $\Gamma^{\mathbf{X}}$ and particle positions \mathbf{X} (material coordinates), deformed to a configuration occupying a region $\Omega^{\mathbf{x}}$ with boundary $\Gamma^{\mathbf{x}}$ and particle positions \mathbf{x} . If the deformation is one-to-one \mathbf{x} is defined by a mapping function $\mathbf{x} = \boldsymbol{\varphi}(\mathbf{X}, t)$ which is a function of the original particle position \mathbf{X} as well as time t . The displacement \mathbf{u} in the current configuration is defined by the difference between its current coordinates in $\Omega^{\mathbf{x}}$, and initial material coordinates in $\Omega^{\mathbf{X}}$:

$$\mathbf{u} = \mathbf{x} - \mathbf{X}. \quad (39)$$

4.2 Governing equations

For thermoplasticity, we decompose the free energy function into an elastic energy ϕ^e , a plastic energy ϕ^p due to work hardening, and thermal energy ϕ^θ following [46]:

$$\phi = \phi^e(\mathbf{F}^e, \theta) + \phi^p(v, \theta) + \phi^\theta(\theta) \quad (40)$$

where \mathbf{F}^e is the elastic deformation gradient, and v is the hardening variable. The entropy for large strain can be expressed as:

$$\eta - \eta^p = -\frac{\partial\phi}{\partial\theta} = -\frac{\partial(\phi^e + \phi^p + \phi^\theta)}{\partial\theta} \quad (41)$$

and

$$\dot{\eta} = \dot{\eta}^p - c_p \dot{\theta} \quad (42)$$

where $c_p = \frac{\partial^2\phi}{\partial\theta^2}\theta$ is the specific heat capacity.

Assuming the free energy function (40) and the entropy (41), the following equations are obtained (see Appendix B for assumptions) for thermoplasticity

$$\rho c_p \dot{\theta} = -\nabla \cdot \mathbf{q} + Q + \chi \dot{w}^p \quad (43)$$

where $\chi \in [0, 1]$ is the Taylor-Quinney coefficient, and $\dot{w}^p = \text{dev}(\boldsymbol{\sigma}) : \dot{\boldsymbol{\epsilon}}^p$ is the plastic power; $\text{dev}(\boldsymbol{\sigma}) = \boldsymbol{\sigma} - \text{trace}(\boldsymbol{\sigma})\mathbb{I}$ is the deviatoric portion of the Cauchy stress, and $\dot{\boldsymbol{\epsilon}}^p$ is the rate of plastic strain.

The classical Fourier heat flux is employed in this work with the scalar (isotropic) thermal conductivity denoted k :

$$\mathbf{q} = -k\nabla\theta. \quad (44)$$

Substituting (44) into (43), the following energy equation is obtained:

$$\rho c_p \dot{\theta} = \nabla \cdot k\nabla\theta + Q + \chi \dot{w}^p. \quad (45)$$

Obviously, the above equation implies an infinite speed for propagation of temperature information. To remedy the fact that this is physically unacceptable, and to facilitate efficient explicit calculations, a thermal sound speed can be introduced into the finite-strain problem. Here, we consider Cattaneo heat conduction [9] (or so-called relativistic heat conduction, which can also be attributed to Vernotte [52] and Chester [20]), which is directly analogous to the modified Fourier law (15):

$$\tau \dot{\mathbf{q}} + \mathbf{q} = k\nabla\theta, \quad (46)$$

where τ is the relaxation time.

Using (46), we obtain a hyperbolic energy equation as

$$\rho c_p \tau \ddot{\theta} + \rho c_p \dot{\theta} = \nabla \cdot k\nabla\theta + Q + \tau \dot{Q} + \chi \dot{w}^p \quad (47)$$

where \dot{Q} comes from Cattaneo conduction. Note that if $\tau = 0$, then the parabolic energy equation (45) is recovered.

For the Cauchy stress, $\boldsymbol{\sigma}$, the Duhamel-Neumann law is adopted:

$$\boldsymbol{\sigma} = \mathbb{C} : (\boldsymbol{\epsilon} - \boldsymbol{\epsilon}^p - \boldsymbol{\epsilon}^\theta) \quad (48)$$

where $\boldsymbol{\epsilon}$, $\boldsymbol{\epsilon}^p$, and $\boldsymbol{\epsilon}^\theta = \bar{\alpha}\theta\mathbb{I}$ are the total, plastic, and thermal strains, respectively ($\boldsymbol{\epsilon} - \boldsymbol{\epsilon}^p - \boldsymbol{\epsilon}^\theta$ is the elastic strain).

Finally, the governing equations of the conservation of linear momentum and the hyperbolic energy equation in the current configuration can be written as

$$\rho \ddot{\mathbf{u}} = \nabla_{\mathbf{x}} \cdot \boldsymbol{\sigma} + \mathbf{b} \quad \text{in } \Omega^{\mathbf{x}} \times]0, t_f[\quad (49a)$$

$$\rho c_p \tau \ddot{\theta} + \rho c_p \dot{\theta} = \nabla_{\mathbf{x}} \cdot k \nabla_{\mathbf{x}} \theta + Q + \tau \dot{Q} + \chi \dot{w}^p \quad \text{in } \Omega^{\mathbf{x}} \times]0, t_f[\quad (49b)$$

where as before, $\nabla_{\mathbf{x}}$ is the Del operator associated with current coordinates \mathbf{x} . As can be seen, the coupling between the two fields arises from the thermal strains and possible dependence of the yield function on temperature (temperature to mechanical), and the plastic power (mechanical to temperature).

4.3 Weak form of thermoplasticity

RKPM employs the weak forms of the governing equations (49). Applying the weighted residual method, integration-by-parts, and the divergence theorem, the weak forms are derived as: find $\mathbf{u} \in U_g^{\mathbf{x}}$, and $\theta \in \Theta_T^{\mathbf{x}}$, such that for all $\mathbf{v} \in U_0^{\mathbf{x}}$, and $S \in \Theta_0^{\mathbf{x}}$ the following equations hold:

$$\int_{\Omega^{\mathbf{x}}} \rho \mathbf{v} \cdot \ddot{\mathbf{u}} d\Omega + \int_{\Omega^{\mathbf{x}}} \nabla_{\mathbf{x}}^s \mathbf{v} : \boldsymbol{\sigma} d\Omega = \int_{\Omega^{\mathbf{x}}} \mathbf{v} \cdot \mathbf{b} d\Omega + \int_{\Gamma_h^{\mathbf{x}}} \mathbf{v} \cdot \mathbf{h} d\Gamma, \quad (50a)$$

$$\begin{aligned} \int_{\Omega^{\mathbf{x}}} \rho c_p \tau S \ddot{\theta} d\Omega + \int_{\Omega^{\mathbf{x}}} \rho c_p S \dot{\theta} d\Omega + \int_{\Omega^{\mathbf{x}}} k \nabla_{\mathbf{x}} S \cdot \nabla_{\mathbf{x}} \theta d\Omega = \\ \int_{\Omega^{\mathbf{x}}} S \chi \dot{w}^p d\Omega + \int_{\Omega^{\mathbf{x}}} S (Q + \tau \dot{Q}) d\Omega + \int_{\Gamma_q^{\mathbf{x}}} S \bar{q} d\Gamma. \end{aligned} \quad (50b)$$

where $\nabla_{\mathbf{x}}^s$ is the symmetric part of $\nabla_{\mathbf{x}}$, $U_g^{\mathbf{x}} = \{\mathbf{u} \mid \mathbf{u} \in H^1, \mathbf{u} = \mathbf{g} \text{ on } \Gamma_g^{\mathbf{x}} \times]0, t_f[\}$, $\Theta_T^{\mathbf{x}} = \{\theta \mid \theta \in H^1, \theta = \bar{\theta} \text{ on } \Gamma_T^{\mathbf{x}} \times]0, t_f[\}$, $U_0^{\mathbf{x}} = \{\mathbf{v} \mid \mathbf{v} \in H^1, \mathbf{v} = \mathbf{0} \text{ on } \Gamma_g^{\mathbf{x}} \times]0, t_f[\}$, and $\Theta_0^{\mathbf{x}} = \{S \mid S \in H^1, S = 0 \text{ on } \Gamma_T^{\mathbf{x}} \times]0, t_f[\}$.

4.4 Galerkin approximation

The Galerkin approximation of (50) asks to find $\mathbf{u}^h \in U^h \subset U_g^{\mathbf{x}}$ and $\theta^h \in \Theta_T^h \subset \Theta_T^{\mathbf{x}}$, such that for all $\mathbf{v}^h \in V^h \subset U_0^{\mathbf{x}}$ and $S^h \in \Theta_0^h \subset \Theta_0^{\mathbf{x}}$ the following equations hold:

$$\int_{\Omega^{\mathbf{x}}} \rho \mathbf{v}^h \cdot \ddot{\mathbf{u}}^h d\Omega + \int_{\Omega^{\mathbf{x}}} \nabla_{\mathbf{x}}^s \mathbf{v}^h : \boldsymbol{\sigma} d\Omega = \int_{\Omega^{\mathbf{x}}} \mathbf{v}^h \cdot \mathbf{b} d\Omega + \int_{\Gamma_h^{\mathbf{x}}} \mathbf{v}^h \cdot \mathbf{h} d\Gamma, \quad (51a)$$

$$\begin{aligned} \int_{\Omega^{\mathbf{x}}} \rho c_p \tau S^h \ddot{\theta}^h d\Omega + \int_{\Omega^{\mathbf{x}}} \rho c_p S^h \dot{\theta}^h d\Omega + \int_{\Omega^{\mathbf{x}}} k \nabla_{\mathbf{x}} S^h \cdot \nabla_{\mathbf{x}} \theta^h d\Omega = \\ \int_{\Omega^{\mathbf{x}}} S^h \chi \dot{w}^p d\Omega + \int_{\Omega^{\mathbf{x}}} S^h (Q + \tau \dot{Q}) d\Omega + \int_{\Gamma_q^{\mathbf{x}}} S^h \bar{q} d\Gamma. \end{aligned} \quad (51b)$$

4.5 Finite-strain RK formulation

4.5.1 Lagrangian RK approximation

The Lagrangian reproducing kernel approximation is constructed with reference to the material configuration \mathbf{X} . Following procedures analogous to Section 3.7, the

shape functions are obtained as [15, 14]:

$$\Psi_I(\mathbf{X}) = \mathbf{H}^\top(\mathbf{0})\mathbf{M}^{-1}(\mathbf{X})\mathbf{H}(\mathbf{X} - \mathbf{X}_I)\phi_a(\mathbf{X} - \mathbf{X}_I) \quad (52)$$

where \mathbf{X}_I is the nodal coordinate in the material configuration.

For the Lagrangian approximation, the displacement and temperature change are constructed (in 2-D as before) as:

$$\mathbf{u}^h(\mathbf{X}) = \sum_{I=1}^{NP} \mathbf{N}_I(\mathbf{X})\mathbf{u}_I, \quad \theta^h(\mathbf{X}) = \sum_{I=1}^{NP} \Psi_I(\mathbf{X})\theta_I \quad (53)$$

where

$$\mathbf{N}_I(\mathbf{X}) = \begin{bmatrix} \Psi_I(\mathbf{X}) & 0 \\ 0 & \Psi_I(\mathbf{X}) \end{bmatrix}, \quad (54)$$

and the test functions are approximated as

$$\mathbf{v}^h(\mathbf{X}) = \sum_{I=1}^{NP} \mathbf{N}_I(\mathbf{X})\mathbf{v}_I, \quad S^h(\mathbf{X}) = \sum_{I=1}^{NP} \Psi_I(\mathbf{X})S_I \quad (55)$$

where $\{\Psi_I(\mathbf{X})\}_{I=1}^{NP}$ are the Lagrangian RK shape functions (52), and \mathbf{u}_I , θ_I , \mathbf{v}_I , and S_I are the nodal coefficients in the Galerkin equation.

4.5.2 Stabilized non-conforming nodal integration (SNNI)

While the formulation of the VC correction technique is straight-forward, the actual coding for large-scale three-dimensional nonlinear codes is somewhat non-trivial. An alternative is to use SCNI [16] which uses conforming cells to satisfy the VC constraints. The main idea of SCNI is to replace the nodal gradient by a smoothed gradient constructed via a Voronoi diagram, as shown in Figure 1, to avoid instability from DNI and inherently satisfy the first-order VC conditions. However, this implementation is also somewhat non-trivial in three-dimensions due to data structures and book-keeping needed. Instead, the stabilized non-conforming nodal integration (SNNI) [25, 26] is adopted here, which utilizes non-conforming cells with a sphere or brick shape as shown in Figure 1.

In SNNI, a direct gradient $\nabla_{\mathbf{X}}$ is replaced with a smoothed gradient $\tilde{\nabla}_{\mathbf{X}}$, constructed as:

$$\tilde{\nabla}_{\mathbf{X}}(\cdot)|_{\mathbf{X}_L} = \frac{1}{\tilde{W}_L^{\mathbf{X}}} \int_{\tilde{\Omega}_L^{\mathbf{X}}} \nabla_{\mathbf{X}}(\cdot) d\Omega = \frac{1}{\tilde{W}_L^{\mathbf{X}}} \int_{\tilde{\Gamma}_L^{\mathbf{X}}} (\cdot) \tilde{\mathbf{n}}^{\mathbf{X}} d\Gamma \quad (56)$$

where \mathbf{X}_L is the nodal point, $\tilde{\Omega}_L^{\mathbf{X}}$ is the smoothing domain associated with each node in the material configuration with boundary $\tilde{\Gamma}_L^{\mathbf{X}}$, $\tilde{W}_L^{\mathbf{X}} \equiv |\tilde{\Omega}_L^{\mathbf{X}}|$ is the smoothing weight of the nodal domain, and $\tilde{\mathbf{n}}^{\mathbf{X}}$ is the unit normal to the nodal smoothing domain. Here, the gradient at a nodal location (as in nodal integration) is smoothed over its representative nodal domain and then the domain integral is converted to a surface integral using the divergence theorem. While relaxation of the conforming condition on the smoothing cells results in loss of variational consistency, so long as the domain is sufficiently uniform, optimal convergence can be achieved [4]. In this work, we

utilize semi-uniform discretizations in the numerical examples. The VC corrections should be implemented if accuracy is desired across all types of discretizations, as shown in Part I.

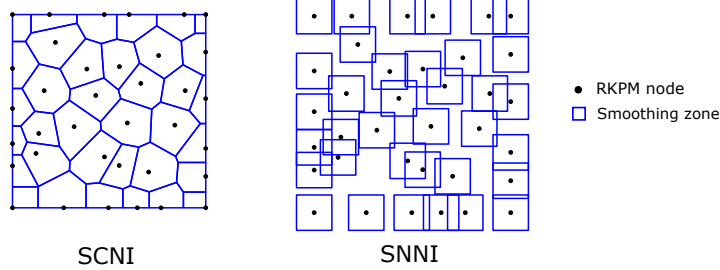


Figure 1: Smoothing cells: conforming nodal integration with SCNI and non-conforming nodal integration with SNNI.

When SNNI is applied to nodal gradient terms, the following approximations result (all smoothed quantities and related variables are denoted with a tilde ($\tilde{\cdot}$) herein):

$$\begin{aligned}\tilde{\boldsymbol{\varepsilon}}(\mathbf{u}^h(\mathbf{X}_L)) &= \sum_{I=1}^{NP} \tilde{\mathbf{B}}_I^u(\mathbf{X}_L) \mathbf{u}_I, & \tilde{\nabla} \theta^h(\mathbf{X}_L) &= \sum_{I=1}^{NP} \tilde{\mathbf{B}}_I^\theta(\mathbf{X}_L) \theta_I \\ \tilde{\boldsymbol{\varepsilon}}(\mathbf{v}^h(\mathbf{X}_L)) &= \sum_{I=1}^{NP} \tilde{\mathbf{B}}_I^v(\mathbf{X}_L) \mathbf{v}_I, & \tilde{\nabla} S^h(\mathbf{X}_L) &= \sum_{I=1}^{NP} \tilde{\mathbf{B}}_I^S(\mathbf{X}_L) S_I\end{aligned}\tag{57}$$

where

$$\begin{aligned}\tilde{\mathbf{B}}_I^u(\mathbf{X}_L) &= \begin{bmatrix} \tilde{b}_{1I}^L & 0 \\ 0 & \tilde{b}_{2I}^L \\ \tilde{b}_{2I}^L & \tilde{b}_{1I}^L \end{bmatrix}, \\ \tilde{\mathbf{B}}_I^\theta(\mathbf{X}_L) &= [\tilde{b}_{1I}^L, \tilde{b}_{2I}^L]^\top, \\ \tilde{b}_{iI}^L &= \frac{1}{\tilde{W}_L^{\mathbf{X}}} \int_{\tilde{\Gamma}_L^{\mathbf{X}}} \Psi_I \tilde{n}_i^{\mathbf{X}} d\Gamma\end{aligned}\tag{58}$$

In the updated Lagrangian formulation, the spatial gradients are required, and here are computed using the smoothed gradient approximation [18]:

$$\begin{aligned}\tilde{\nabla}_{\mathbf{x}} \otimes \mathbf{u}^h(\mathbf{X}_L) &= \frac{\partial \mathbf{X}}{\partial \mathbf{x}}(\mathbf{X}_L) \cdot \left(\tilde{\nabla}_{\mathbf{X}} \otimes \mathbf{u}^h(\mathbf{X}_L) \right) \approx \tilde{\mathbf{F}}(\mathbf{X}_L)^{-\top} \cdot \left(\tilde{\nabla}_{\mathbf{X}} \otimes \mathbf{u}^h(\mathbf{X}_L) \right), \\ \tilde{\nabla}_{\mathbf{x}} \theta(\mathbf{X}_L) &= \frac{\partial \mathbf{X}}{\partial \mathbf{x}}(\mathbf{X}_L) \cdot \left(\tilde{\nabla}_{\mathbf{X}} \theta(\mathbf{X}_L) \right) \approx \tilde{\mathbf{F}}(\mathbf{X}_L)^{-\top} \cdot \left(\tilde{\nabla}_{\mathbf{X}} \theta(\mathbf{X}_L) \right),\end{aligned}\tag{59}$$

where the smoothed deformation gradient $\tilde{\mathbf{F}}$ is computed as:

$$\tilde{\mathbf{F}}(\mathbf{X}_L) = \mathbf{I} + \sum_{I=1}^{NP} \tilde{\nabla}_{\mathbf{X}} \Psi_I(\mathbf{X}_L) \otimes \mathbf{u}_I.\tag{60}$$

For the inverse of the deformation gradient $\tilde{\mathbf{F}}^{-1}$, the mapping must exist between the undeformed and deformed configuration. For material separation where the mapping does not exist everywhere, the semi-Lagrangian formulation can be introduced [26]. In this work, the Lagrangian approximation (52) is employed since the deformations are not severe in the chosen benchmarks.

Finally, we note for nodal quadrature of the Updated Lagrangian formulation, nodal weights in the current configuration also employ $\tilde{\mathbf{F}}$ and are computed as $W_L^x = \det(\tilde{\mathbf{F}})W_L^X$ where W_L^X is the weight in the undeformed configuration.

4.6 Naturally stabilized nodal integration in thermoplasticity

In this section, the nodal stabilization given in Part I is extended to nonlinear problems. Most of the procedures are a straightforward analogy, so particular emphasis is only given to key differences. Here as in the rest of the text, two dimensions are considered without loss of generality.

4.6.1 Stabilization of the mechanical field

To start, the variation on strains in nodal domains are expanded about the current nodal position \mathbf{x}_L using a Taylor series expansion truncated to first order [27]:

$$\boldsymbol{\varepsilon}(\mathbf{v}^h) \approx \boldsymbol{\varepsilon}_L(\mathbf{v}^h) + \sum_{i=1}^2 \{(x_i - x_{Li})\boldsymbol{\varepsilon}_L(\mathbf{v}^h)_{,i}\}. \quad (61)$$

where $\boldsymbol{\varepsilon}_L(\mathbf{v}^h) \equiv \boldsymbol{\varepsilon}(\mathbf{v}^h(\mathbf{x}_L))$ and $(\)_{,i} \equiv \partial(\)/\partial x_i$. Now, rather than the strain, the Cauchy stress is instead expanded:

$$\boldsymbol{\sigma}(\mathbf{u}^h) \approx \boldsymbol{\sigma}_L(\mathbf{u}^h) + \sum_{i=1}^2 \{(x_i - x_{Li})\boldsymbol{\sigma}_L(\mathbf{u}^h)_{,i}\}. \quad (62)$$

where $\boldsymbol{\sigma}_L(\mathbf{u}^h) \equiv \boldsymbol{\sigma}(\mathbf{u}^h(\mathbf{x}_L))$. As in Part I, we have considered the linear ($n = 1$) case and only retain first-order terms. Substituting (61) and (62) into (51a) with nodal quadrature and employing the smoothed (56) and implicit (30) gradient approximations, the following smoothed naturally stabilized nodal quadrature version of the bilinear form is obtained as:

$$a_{SN}^x \langle \mathbf{v}^h, \mathbf{u}^h \rangle = a_S^x \langle \mathbf{v}^h, \mathbf{u}^h \rangle + a_N^x \langle \mathbf{v}^h, \mathbf{u}^h \rangle \quad (63)$$

where $a_S^x \langle \cdot, \cdot \rangle$ is the SNNI quadrature version of the bilinear form using strain smoothing:

$$a_S^x \langle \mathbf{v}^h, \mathbf{u}^h \rangle = \sum_{L=1}^{NP} \tilde{\boldsymbol{\varepsilon}}_L(\mathbf{v}^h) : \tilde{\boldsymbol{\sigma}}_L(\mathbf{u}^h) W_L^x \quad (64)$$

where $\tilde{\boldsymbol{\sigma}}$ denotes the Cauchy stress computed using the smoothed strain, and the stabilization term $a_N^x \langle \cdot, \cdot \rangle$ is

$$a_N^x \langle \mathbf{v}^h, \mathbf{u}^h \rangle = \sum_{L=1}^{NP} \sum_{i=1}^2 \hat{\boldsymbol{\varepsilon}}_{Li}(\mathbf{v}^h) : \tilde{\boldsymbol{\sigma}}_{Li}(\mathbf{u}^h) M_{Li}^x \quad (65)$$

where $\hat{\boldsymbol{\varepsilon}}_{L\bar{i}}(\mathbf{v}^h)$ is the smoothed implicit gradient approximation of $\boldsymbol{\varepsilon}_L(\mathbf{v}^h)_{,\bar{i}}$, $\tilde{\boldsymbol{\sigma}}_{L\bar{i}}(\mathbf{u}^h)$ is the approximation to $\boldsymbol{\sigma}_L(\mathbf{u}^h)_{,\bar{i}}$ using $\hat{\boldsymbol{\varepsilon}}_{L\bar{i}}(\mathbf{u}^h)$ and

$$M_{Li}^{\mathbf{x}} = \int_{\Omega_L^{\mathbf{x}}} (x_i - x_{Li})^2 d\Omega, \quad (66)$$

which are the second moments of inertia of each integration zone in the current configuration. For the Lagrangian formulation, to avoid recomputing the spatial moments in (66), these are pre-computed just as other quantities, and are approximated at the current time step by:

$$M_{Li}^{\mathbf{x}} \approx \det(\tilde{\mathbf{F}}(\mathbf{X}_I)) \int_{\Omega_L^{\mathbf{X}}} (X_i - X_{Li})^2 d\Omega. \quad (67)$$

The smoothed nodal terms in (64) are constructed using SNNI as in (57). Additional terms containing the derivatives of strains are approximated by *smoothed* implicit gradients (in contrast to Part I) as

$$\begin{aligned} \hat{\boldsymbol{\varepsilon}}_{L\bar{i}}(\mathbf{u}^h) &= \sum_{I=1}^{NP} \mathbf{B}_{I\bar{i}}^{u\tilde{\nabla}}(\mathbf{x}_L) \mathbf{u}_I, & \hat{\boldsymbol{\varepsilon}}_{L\bar{i}}(\mathbf{v}^h) &= \sum_{I=1}^{NP} \mathbf{B}_{I\bar{i}}^{v\tilde{\nabla}}(\mathbf{x}_L) \mathbf{v}_I, \\ \mathbf{B}_{I\bar{i}}^{u\tilde{\nabla}}(\mathbf{x}) &= \begin{bmatrix} \Psi_{I\bar{i}1}^{\tilde{\nabla}}(\mathbf{x}) & 0 \\ 0 & \Psi_{I\bar{i}2}^{\tilde{\nabla}}(\mathbf{x}) \\ \Psi_{I\bar{i}2}^{\tilde{\nabla}}(\mathbf{x}) & \Psi_{I\bar{i}1}^{\tilde{\nabla}}(\mathbf{x}) \end{bmatrix} \end{aligned} \quad (68)$$

where the spatial derivatives $\Psi_{I\bar{i}j}$ are mapped as in (59) from

$$\Psi_{I\bar{i}j}^{\tilde{\nabla}} = \frac{1}{2\tilde{W}_L^{\mathbf{X}}} \int_{\tilde{\Gamma}_L^{\mathbf{X}}} (\Psi_{I\bar{i}}^{\nabla} \tilde{n}_j^{\mathbf{X}} + \Psi_{I\bar{i}j}^{\nabla} \tilde{n}_i^{\mathbf{X}}) d\Gamma. \quad (69)$$

The above averaging enforces the mathematical property of true second-order derivatives $\Psi_{I\bar{i}j}^{\tilde{\nabla}} = \Psi_{I\bar{i}j}^{\tilde{\nabla}}$.

Note that in this formulation, no direct derivatives are involved, which is computationally efficient. Further details and enhanced algorithms for smoothed Lagrangian natural stabilization will be presented in a forthcoming paper.

Finally, the stress updates in this paper follow the Hughes-Winget algorithm [32] in order to maintain objectivity, while the updates of the derivative of stresses in (62) use the strains in (68) following the procedure given in the Appendix of [27].

4.6.2 Stabilization of temperature field

Following the procedures for the displacement field, expanding the temperature gradient in nodal domains is proposed in this work to achieve stabilization of the temperature field:

$$\nabla_{\mathbf{x}} \theta^h(\mathbf{x}) \approx \nabla_{\mathbf{x}} \theta_L^h + \sum_{i=1}^2 \{(x_i - x_{Li})(\nabla_{\mathbf{x}} \theta_L^h)_{,\bar{i}}\} \quad (70)$$

where $\nabla_{\mathbf{x}}\theta_L^h \equiv \nabla_{\mathbf{x}}\theta^h(\mathbf{x}_L)$. The test function gradient follows the same form:

$$\nabla_{\mathbf{x}}S^h(\mathbf{x}) \approx \nabla_{\mathbf{x}}S_L^h + \sum_{i=1}^2 \{(x_i - x_{I_i})(\nabla_{\mathbf{x}}S_L^h)_{,\bar{i}}\} \quad (71)$$

where $\nabla_{\mathbf{x}}S_L^h \equiv \nabla_{\mathbf{x}}S^h(\mathbf{x}_L)$.

Employing (70) and (71) in (51b) with nodal quadrature and employing the smoothed (56) and implicit (30) gradient approximations, the following stabilized bilinear form is obtained for the temperature field:

$$\bar{a}_{SN}^{\mathbf{x}} \langle S^h, \theta^h \rangle = \bar{a}_S^{\mathbf{x}} \langle S^h, \theta^h \rangle + \bar{a}_N^{\mathbf{x}} \langle S^h, \theta^h \rangle \quad (72)$$

where $\bar{a}_S^{\mathbf{x}} \langle \cdot, \cdot \rangle$ is the SNNI quadrature version of the bilinear form using gradient smoothing (56):

$$\bar{a}_S^{\mathbf{x}} \langle S^h, \theta^h \rangle = \sum_{L=1}^{NP} k(\tilde{\nabla}_{\mathbf{x}}S_L^h) \cdot (\tilde{\nabla}_{\mathbf{x}}\theta_L^h)M_{Li}^{\mathbf{x}} \quad (73)$$

and the stabilization term for temperature $\bar{a}_N^{\mathbf{x}} \langle \cdot, \cdot \rangle$ is computed as

$$\bar{a}_N^{\mathbf{x}} \langle S^h, \theta^h \rangle = \sum_{L=1}^{NP} \sum_{i=1}^2 k(\hat{\nabla}S_{L\bar{i}}^h) \cdot (\hat{\nabla}\theta_{L\bar{i}}^h)M_{Li} \quad (74)$$

where $\hat{\nabla}S_{L\bar{i}}^h$ and $\hat{\nabla}\theta_{L\bar{i}}^h$ denote the smoothed implicit approximations to $\nabla S_{L,\bar{i}}^h$ and $\nabla\theta_{L,\bar{i}}^h$, respectively.

The nodal gradients in the SNNI term are computed using (57). For the stabilization terms in (74), smoothed implicit gradients are utilized as follows:

$$\begin{aligned} \hat{\nabla}S_{L\bar{i}}^h &= \sum_{I=1}^{NP} \mathbf{B}_{I\bar{i}}^{\theta\hat{\nabla}}(\mathbf{x}_L)S_I, & \hat{\nabla}\theta_{L\bar{i}}^h &= \sum_{I=1}^{NP} \mathbf{B}_{I\bar{i}}^{\theta\hat{\nabla}}(\mathbf{x}_L)\theta_I, \\ \mathbf{B}_{I\bar{i}}^{\theta\hat{\nabla}}(\mathbf{x}) &= [\Psi_{I\bar{i}1}^{\hat{\nabla}}(\mathbf{x}) \quad \Psi_{I\bar{i}2}^{\hat{\nabla}}(\mathbf{x})]^{\top}. \end{aligned} \quad (75)$$

Note that the weights $W_L^{\mathbf{x}}$ and second moments of inertia $M_{Li}^{\mathbf{x}}$ are the same as in Section 4.6.1.

4.7 Semi-discrete matrix equations

Herein, we consider the explicit formulation for thermoplasticity. First, the semi-discrete form using SNNI and NSNI can be stated as:

$$\mathbf{M}_u \mathbf{a}_u(t) = \mathbf{f}_u^{\text{ext}}(t) - \mathbf{f}_u^{\text{int}}(t) \quad (76a)$$

$$\mathbf{M}_\theta \mathbf{a}_\theta(t) + \mathbf{C}_\theta \mathbf{v}_\theta(t) = \mathbf{f}_\theta^{\text{ext}}(t) + \mathbf{f}_\theta^{\text{diss}}(t) - \mathbf{f}_\theta^{\text{int}}(t) \quad (76b)$$

where we have adopted the notation $\mathbf{a}_u \equiv \ddot{\mathbf{u}}$, $\mathbf{v}_u \equiv \dot{\mathbf{u}}$, $\mathbf{d}_u \equiv \mathbf{u}$, $\mathbf{a}_\theta \equiv \ddot{\boldsymbol{\theta}}$, $\mathbf{v}_\theta \equiv \dot{\boldsymbol{\theta}}$, and $\mathbf{d}_\theta \equiv \boldsymbol{\theta}$; \mathbf{u} and $\boldsymbol{\theta}$ are the row vectors of $\{\mathbf{u}_I\}_{I=1}^{NP}$ and $\{\theta_I\}_{I=1}^{NP}$, respectively, and the

matrix entries of the above are

$$\mathbf{M}_{uIJ} = \sum_{L=1}^{NP} \rho(\mathbf{X}_L) \bar{\mathbf{I}} \Psi_I(\mathbf{X}_L) \Psi_J(\mathbf{X}_L) W_L^x \quad (77a)$$

$$M_{\theta IJ} = \sum_{L=1}^{NP} \tau \rho(\mathbf{X}_L) c_p(\mathbf{X}_L) \Psi_I(\mathbf{X}_L) \Psi_J(\mathbf{X}_L) W_L^x \quad (77b)$$

$$C_{\theta IJ} = \sum_{L=1}^{NP} \rho(\mathbf{X}_L) c_p(\mathbf{X}_L) \Psi_I(\mathbf{X}_L) \Psi_J(\mathbf{X}_L) W_L^x \quad (77c)$$

$$\mathbf{f}_{uI}^{\text{int}} = \sum_{L=1}^{NP} \left((\tilde{\mathbf{B}}_I^u(\mathbf{X}_L))^{\top} \Sigma(\mathbf{X}_L) W_L^x + \sum_{i=1}^2 (\mathbf{B}_i^{u\nabla}(\mathbf{x}_L))^{\top} \Sigma(\mathbf{X}_L)_{,\bar{i}}(\mathbf{x}_L) M_{Li}^x \right) \quad (77d)$$

$$\mathbf{f}_{uI}^{\text{ext}} = \sum_{K=1}^{NBPu} \Psi_I(\mathbf{x}_K) \mathbf{h}(\mathbf{X}_K) L_K^u + \sum_{L=1}^{NP} \Psi_I(\mathbf{X}_L) \mathbf{b}(\mathbf{X}_L) W_L^x \quad (77e)$$

$$f_{\theta I}^{\text{int}} = \sum_{L=1}^{NP} \left((\tilde{\mathbf{B}}_I^{\theta}(\mathbf{X}_L))^{\top} k(\mathbf{X}_L) \tilde{\nabla}_{\mathbf{x}} \theta(\mathbf{X}_L) W_L^x + \sum_{i=1}^2 k(\mathbf{X}_L) (\mathbf{B}_i^{\theta\nabla}(\mathbf{x}_L))^{\top} \hat{\nabla} \theta_{L\bar{i}}^h M_{Li}^x \right) \quad (77f)$$

$$f_{\theta I}^{\text{ext}} = \sum_{K=1}^{NBP\theta} \Psi_I(\mathbf{x}_K) q(\mathbf{X}_K) L_K^{\theta} + \sum_{L=1}^{NP} \Psi_I(\mathbf{X}_L) (Q(\mathbf{X}_L) + \tau Q(\dot{\mathbf{X}}_L)) W_L^x \quad (77g)$$

$$f_{\theta I}^{\text{diss}} = \sum_{L=1}^{NP} \Psi_I(\mathbf{X}_L) \chi \dot{w}^p(\mathbf{X}_L) W_L^x \quad (77h)$$

with

$$\bar{\mathbf{I}} = \begin{bmatrix} 1 & 0 \\ 0 & 1 \end{bmatrix}, \quad (78)$$

$$\Sigma(\mathbf{X}_L) = [\tilde{\sigma}_{11}(\mathbf{X}_L), \tilde{\sigma}_{22}(\mathbf{X}_L), \tilde{\sigma}_{12}(\mathbf{X}_L)]^{\top},$$

\mathbf{b} and \mathbf{h} are the matrix forms of \mathbf{b} and \mathbf{h} , respectively, and L_K^u and L_K^{θ} denote the K th weight of one of the $NBPu$ and $NBP\theta$ integration points on the natural boundaries for the displacement and temperature change in the current configuration, respectively. As described in Section 4.6, the stress gradient $\Sigma(\mathbf{X}_L)_{,\bar{i}}$ is not computed directly but instead approximated.

4.8 Fully discrete matrix equations for explicit hyperbolic analysis

In this section, we introduce the fully discrete matrix equations for explicit hyperbolic analysis following the Newmark method with the central difference scheme [31]. For the parabolic version, the heat equation just follows the forward Euler algorithm on temperature. First, denote the approximation of displacement variables at time t_n as $\mathbf{a}_u^n \approx \mathbf{a}_u(t_n)$, $\mathbf{v}_u^n \approx \mathbf{v}_u(t_n)$, and $\mathbf{d}_u^n \approx \mathbf{d}_u(t_n)$.

The approximate temperature changes and their rates at t_n are $\mathbf{a}_{\theta}^n \approx \mathbf{a}_{\theta}(t_n)$, $\mathbf{v}_{\theta}^n \approx \mathbf{v}_{\theta}(t_n)$, and $\mathbf{d}_{\theta}^n \approx \mathbf{d}_{\theta}(t_n)$. Then the following algorithm is obtained for the central difference method at time t_{n+1} :

Predictor phase Compute predicted quantities ($\hat{\cdot}$):

$$\hat{\mathbf{d}}_u^{n+1} = \mathbf{d}_u^n + \Delta t \mathbf{v}_u^n + \frac{\Delta t^2}{2} \mathbf{a}_u^n, \quad (79a)$$

$$\hat{\mathbf{v}}_u^{n+1} = \mathbf{v}_u^n + \frac{\Delta t}{2} \mathbf{a}_u^n, \quad (79b)$$

$$\hat{\mathbf{d}}_\theta^{n+1} = \mathbf{d}_\theta^n + \Delta t \mathbf{v}_\theta^n + \frac{\Delta t^2}{2} \mathbf{a}_\theta^n, \quad (79c)$$

$$\hat{\mathbf{v}}_\theta^{n+1} = \mathbf{v}_\theta^n + \frac{\Delta t}{2} \mathbf{a}_\theta^n. \quad (79d)$$

Note that in the central difference method, some of the predicted values are the corrected values such that $\mathbf{d}_u^{n+1} = \hat{\mathbf{d}}_u^{n+1}$ and $\mathbf{d}_\theta^{n+1} = \hat{\mathbf{d}}_\theta^{n+1}$. This makes the internal force-type terms possible to compute exactly at any given time step and are thus moved to the right-hand side.

Solve the governing equations Solve for the accelerations and their temperature counterparts from the Governing equations.

For the hyperbolic version, to keep the method explicit, the following "mass" matrices are lumped using the row-sum method, and the predictor for the velocity-type temperature terms are employed and moved to the right-hand side:

$$\mathbf{M}_u^l \mathbf{a}_u^{n+1} = \mathbf{f}_u^{\text{ext}} - \mathbf{f}_u^{\text{int}}, \quad (80a)$$

$$\mathbf{M}_\theta^l \mathbf{a}_\theta^{n+1} = \mathbf{f}_\theta^{\text{ext}} + \mathbf{f}_\theta^{\text{diss}} - \mathbf{f}_\theta^{\text{int}} - \mathbf{C}_\theta \tilde{\mathbf{v}}_\theta^{n+1}. \quad (80b)$$

Since the mass matrices are lumped (80) is simply a set of row equations and needs no solver. Also note, the coupling between mechanical fields and temperature is given by the source term $\dot{\omega}^p$ in the energy equation in $\mathbf{f}_\theta^{\text{diss}}$, the temperature strain in the Cauchy stress $\boldsymbol{\sigma}$ in $\mathbf{f}_u^{\text{int}}$, and the possible effect of the temperature on the yield stress in plasticity in $\mathbf{f}_u^{\text{int}}$.

Corrector phase Compute corrected quantities:

$$\mathbf{d}_u^{n+1} = \hat{\mathbf{d}}_u^{n+1} \quad (\text{no correction}), \quad (81a)$$

$$\mathbf{v}_u^{n+1} = \hat{\mathbf{v}}_u^{n+1} + \frac{\Delta t}{2} \mathbf{a}_u^{n+1}, \quad (81b)$$

$$\mathbf{d}_\theta^{n+1} = \hat{\mathbf{d}}_\theta^{n+1} \quad (\text{no correction}), \quad (81c)$$

$$\mathbf{v}_\theta^{n+1} = \hat{\mathbf{v}}_\theta^{n+1} + \frac{\Delta t}{2} \mathbf{a}_\theta^{n+1}. \quad (81d)$$

Hence, the algorithm follows the typical explicit scheme for pure solid mechanics, with no special treatments. Therefore existing explicit solids codes can benefit from the present approach if thermomechanical coupling is desired. In addition, when the second sound speed is equated with the first (see the Sections 5 and 6), the time step requirement also remains the same.

5 Time-step criteria

In this section we examine the time-step criteria for the G-L theory using the explicit Newmark Method (the extension to L-S is straightforward), and compare it to the classical theory with the explicit generalized trapezoidal rule (forward Euler) method with lumped mass, as has been used in the past for explicit thermomechanical analysis (e.g., see [43]). We note that the coupled system for the generalized theory (80) is not solved in a matrix fashion monolithically, so we examine the limitation on the time step due to the temperature field alone.

There are three main methods typically considered in stability analysis: (1) modal analysis, (2) the Von Neumann Method, and (3) the energy method. Here we use modal analysis based on linear finite elements (as a proxy for a linear meshfree discretization, with nodal spacing Δx , which is conservative for nodal integration methods [17]) to examine the critical time step, Δt_{cr} . We solve the following problem to determine the maximum magnitude of the element eigenvalues, which governs the time step:

$$(\mathbf{K}^e - \lambda_i^2 \mathbf{M}^e) \boldsymbol{\phi}_i = \mathbf{0}, \quad i = 1, 2 \quad (82)$$

where $\boldsymbol{\phi}_i$ is an eigenvector and λ_i is the associated eigenvalue, and for the element eigenvalue problem:

$$\mathbf{M}^e = \frac{t_2 \rho c_p l^e}{2} \begin{bmatrix} 1 & 0 \\ 0 & 1 \end{bmatrix} \quad \mathbf{K}^e = \frac{k}{l^e} \begin{bmatrix} 1 & -1 \\ -1 & 1 \end{bmatrix}. \quad (83)$$

where l^e is the length of an element. For simplicity, damping is neglected here, since this does not effect the time step estimate with the standard selection of $\gamma = 1/2$, which is needed for second order accuracy [31].

Following standard procedures, one can obtain two solutions:

$$\lambda = 0, \quad \text{and} \quad \lambda = \frac{4k}{t_2 \rho c_p (l^e)^2}. \quad (84)$$

Since $\Delta t_{\text{cr}} = 2/\sqrt{\max(\lambda)}$ in the central difference method [31], the critical time step of the hyperbolic heat equation using lumped mass is:

$$\Delta t \leq \Delta t_{\text{cr}} = \frac{2}{\sqrt{\max(\lambda)}} = \sqrt{\frac{t_2 \rho c_p}{k}} l^e = \frac{l^e}{c_{\text{T,GL}}}, \quad (85)$$

where $c_{\text{T,GL}}$ is the temperature propagation speed for the G-L theory (21). So, the critical time step of the hyperbolic heat equation is $\Delta t_{\text{cr}} \propto l^e$, and mimics the requirement for pure solid mechanics problems. That is, the critical time step is exactly the time it takes for a wave to pass through one element. This time, it is the second sound speed. Therefore for efficiency, relaxation times can be based on equating the second sound speed with the first. This seems to be also a practical solution, since this data is generally unavailable for most materials, and this also results in very small relaxation times yielding results close to the classical theory.

L-S follows a similar derivation, with the critical time step governed by the associated wave speed with

$$\Delta t \leq \Delta t_{\text{cr}} = \frac{l^e}{c_{\text{T,LS}}}. \quad (86)$$

For comparison, using forward Euler with lumped element "heat mass" matrix \mathbf{C}^e (the explicit generalized trapezoidal rule), the critical time step of the classic parabolic theory can be determined using eigenvalue strategies as in (82):

$$(\mathbf{K}^e - \lambda_i^p \mathbf{C}^e) \phi_i^p = \mathbf{0}, \quad i = 1, 2 \quad (87)$$

where ϕ_i^p is an eigenvector and λ_i^p is the associated eigenvalue, and for the element eigenvalue problem:

$$\mathbf{C}^e = \frac{\rho c_p l^e}{2} \begin{bmatrix} 1 & 0 \\ 0 & 1 \end{bmatrix} \quad \mathbf{K}^e = \frac{k}{l^e} \begin{bmatrix} 1 & -1 \\ -1 & 1 \end{bmatrix}. \quad (88)$$

Stability for the Forward Euler algorithm is $\Delta t_{\text{cr}} = 2/\max(\lambda)$ [31]. Thus, the critical time step governed by the associated wave speed with

$$\Delta t \leq \Delta t_{\text{cr}} = \frac{2}{\max(\lambda)} = \frac{(l^e)^2 \rho c_p}{2k} \quad (89)$$

Based on (85), (86) and (89), the time step for parabolic equation will always be smaller than the hyperbolic equation as $l^e \rightarrow 0$.

6 Numerical examples

In this section numerical examples are presented to demonstrate the accuracy of stability of the proposed method. For generalized thermoelasticity, four different integration methods are used for comparison to demonstrate the necessity of both stabilization and variationally consistent integration. Three benchmarks of thermoelasticity and a thermoplastic benchmark are solved, and the results are compared with numerical methods such as FEM and BEM, and experimental data when available.

6.1 Generalized thermoelasticity

In this section the accuracy of stability of the proposed method in generalized thermoelasticity is studied. The following numerical integration methods are employed in this section:

1. Direct nodal integration (denoted DNI)
2. Variationally consistent integration with direct nodal integration (denoted VC-DNI)
3. Naturally stabilized nodal integration (denoted NSNI)
4. Variationally consistent integration with naturally stabilized nodal integration (denoted VC-NSNI)

Unless otherwise stated, for the RK approximation, linear basis with cubic B-spline kernels with a normalized support size of 2 are employed in all problems, using a uniform node distribution with a nodal spacing of $\Delta x = 0.001$. The implicit and unconditionally stable backward difference method [44] is employed with a time step of $\Delta t = 0.001$ to discretize the time domain in all examples in this section. The transformation method [15] is used for the imposition of essential boundary conditions. The solutions are presented in terms of the dimensionless variables

$$\bar{y} = \frac{y}{\bar{a}}, \quad \bar{\theta} = \frac{\theta}{\theta_0}, \quad \bar{t} = \frac{\kappa}{\bar{a}^2}t, \quad \bar{u} = \frac{(\lambda + 2\mu)}{\bar{a}\beta\theta_0}u, \quad \bar{t}_0 = \frac{\kappa}{\bar{a}^2}t_0, \quad \bar{t}_1 = \frac{\kappa}{\bar{a}^2}t_1, \quad \bar{t}_2 = \frac{\kappa}{\bar{a}^2}t_2, \quad (90)$$

where $\bar{a} = \kappa/c_s\rho c_p$; $\kappa = k/\rho c_p$, and $c_s = \sqrt{(\lambda + 2\mu)/\rho}$.

We consider a linear elastic half-space $y \geq 0$ subjected to a uniform sudden temperature change on its boundary plane, free of traction. This initial boundary value problem is the first Danilovskaya's problem [21]. The boundary conditions in this problem are given as

$$\theta(0, t) = \theta_0, \quad (91a)$$

$$\sigma(0, t) = 0. \quad (91b)$$

The above problem can be treated as one-dimensional coupled and uncoupled generalized thermoelasticity. Unless otherwise stated, all material properties used in the studies are given in Table 1, and for the L-S theory, the relaxation time $\bar{t}_0 = 2$ s is used, and for the G-L theory, the relaxation times \bar{t}_1 and \bar{t}_2 are 2.25 s. The full inertial dynamic representation of the problem is employed.

	k	ρ	c_p	β	$\lambda + 2\mu$
value	1.7×10^3	7.82×10^{-3}	4.61×10^6	3.34×10^4	1.99×10^9
unit	kg \times cm/K/s ³	kg/cm ³	cm ² /K/s ³	kg/cm/K/s ²	kg/cm/s ²

Table 1: Parameters for numerical examples in generalized thermoelasticity unless otherwise stated.

6.1.1 Stability and accuracy study

The stability and accuracy of the proposed VC-NSNI method is first studied. Later, the need for both VC and NSNI techniques will be examined and confirmed.

Consider the G-L theory. Figure 2 shows that the comparison of RKPM with BEM [10] and FEM [44] for the coupled ($\delta = 1$) and uncoupled ($\delta = 0$) cases. The results are clearly stable, and both the displacement and temperature change are very close to the BEM and FEM solutions.

Interesting features of this problem include the fact that the peak of displacement in the coupled model is smaller and flatter than uncoupled model. For the temperature change, the coupled results have smaller magnitude, and show a longer delay before the large rise in temperature.

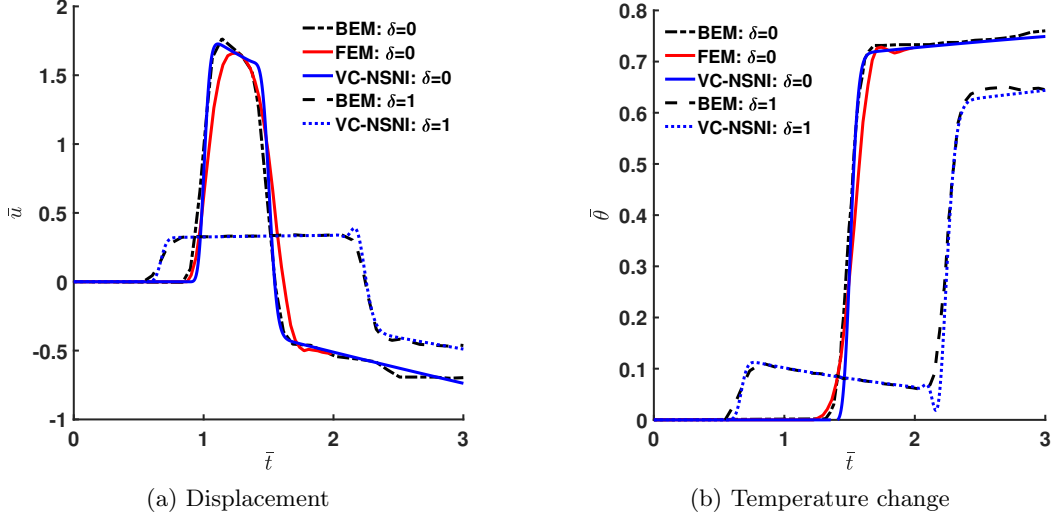


Figure 2: Time histories for the first Danilovskaya problem with the G-L theory.

Figure 3 shows the comparison of RKPM with BEM [10] for the coupled ($\delta = 1$) and uncoupled ($\delta = 0$) cases for the L-S theory. Both displacement and temperature change are stable, and also close to reference results. The temperature change profile is similar to the G-L theory. For the displacement, peaks are easily seen in both the coupled and uncoupled cases, and the transition is well-captured.

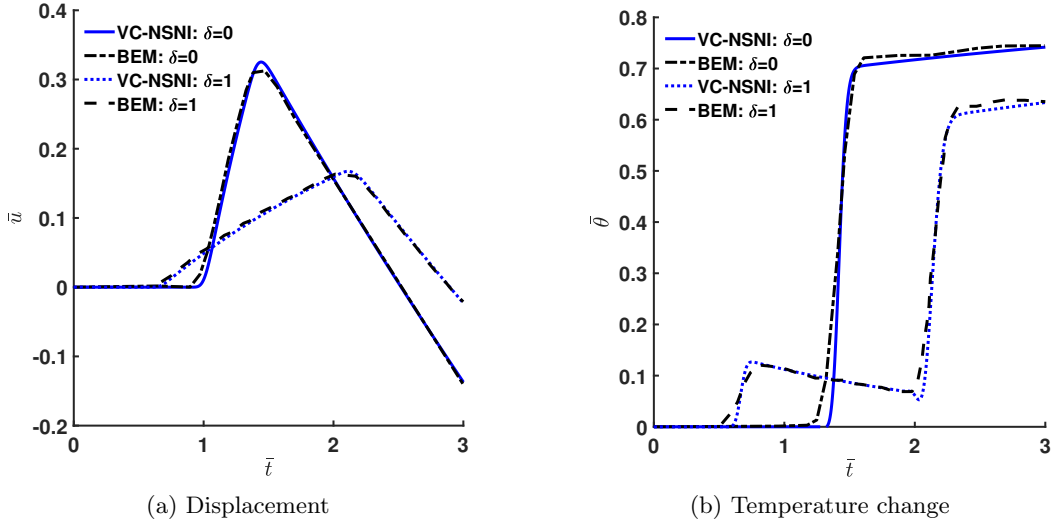


Figure 3: Time histories for the first Danilovskaya problem with the L-S theory.

In summary, the results using RKPM with VC-NSNI are stable for both the G-L and L-S theories, and are close to the available reference solutions.

6.1.2 Node distribution study

A non-uniform discretization is now considered to demonstrate the accuracy of the present approach, and necessity for stabilization and variationally consistent integration. Largely, uniform discretizations (as in the previous example) are special

cases where high accuracy can be obtained in meshfree methods regardless of the quadrature technique (excluding pure nodal integration which is unstable).

Consider a transition ($\Delta x = 0.005, \Delta x = 0.01$) in nodal spacing, as shown in Figure 4. In [28] it was shown that this type of spatial discretization is very challenging for nodal integration in meshfree methods for dynamic problems, so it is selected.



Figure 4: Node distribution with transition in one dimension.

DNI, VC-DNI, NSNI, and VC-NSNI are employed for domain integration. Since the G-L and L-S theories do not have exact solutions, VC-NSNI with a uniform node distribution ($\Delta x = 0.005$) is employed as reference (denoted as Reference).

The time histories for displacement and temperature for the G-L and L-S theories are shown in Figures 5-8. Here it is seen that DNI provides quite spurious behavior in all cases, particularly in displacements. Meanwhile, NSNI and VCI can provide more accuracy in both displacement and temperature compared to DNI. However, each alone can not achieve the accuracy of the reference solution. While NSNI seems to provide fairly acceptable results, there are still some discrepancies later in time ($\bar{t} > 2$). Only when the combined VC-NSNI is employed solutions can be obtained that are very close to the reference solutions for all fields and all cases.

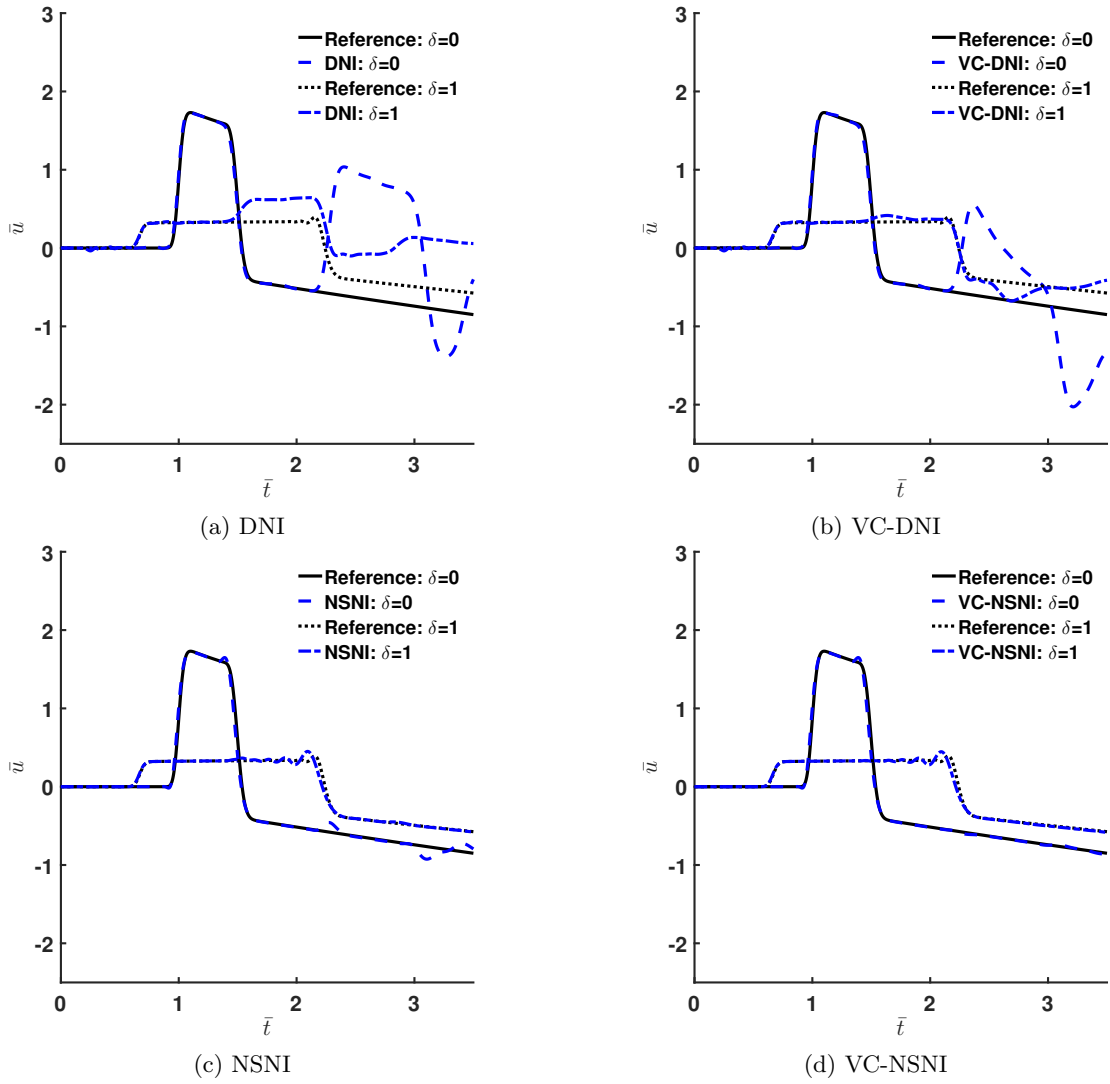


Figure 5: Displacement time histories using the G-L theory with various integration methods.

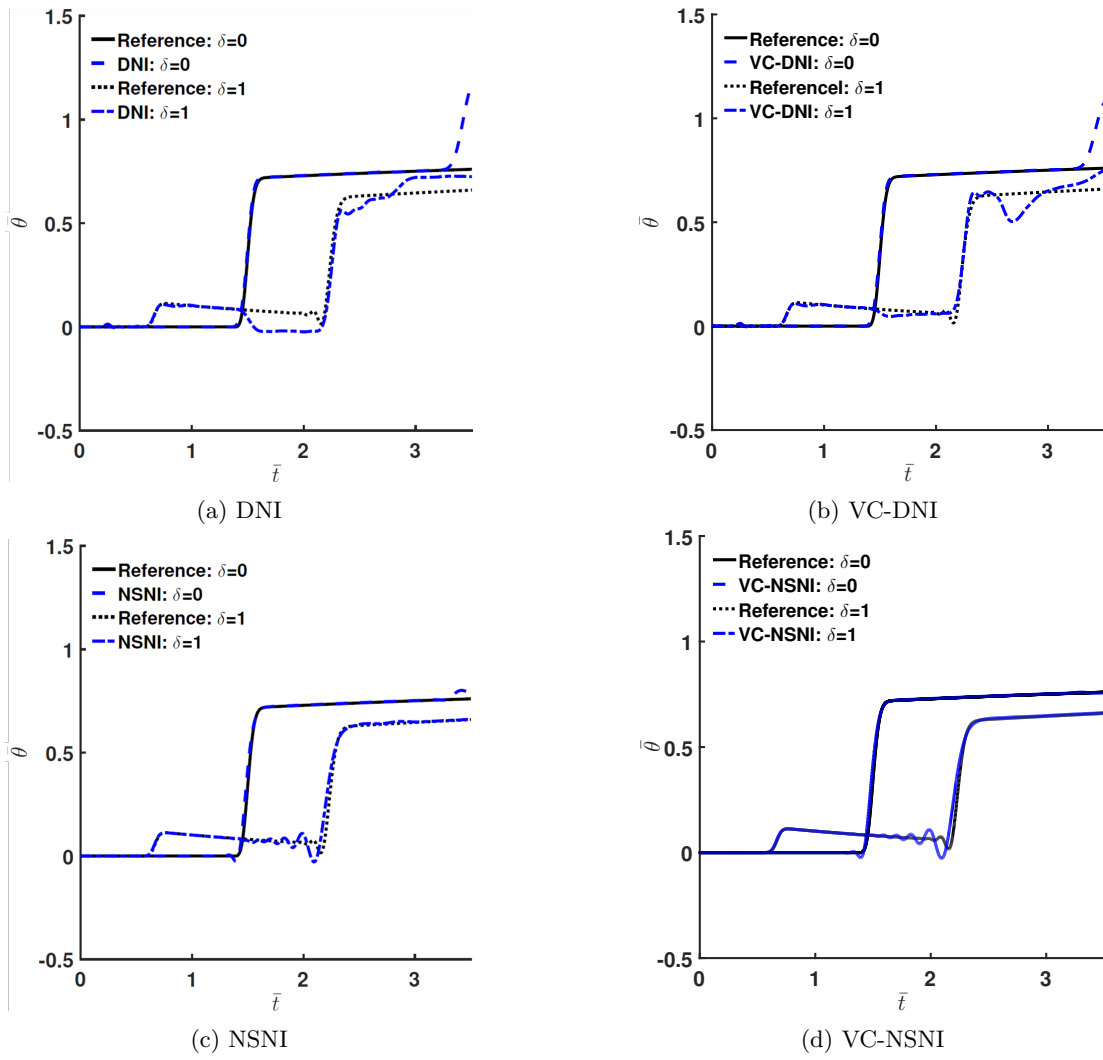


Figure 6: Time histories of temperature change using the G-L theory with various integration methods.

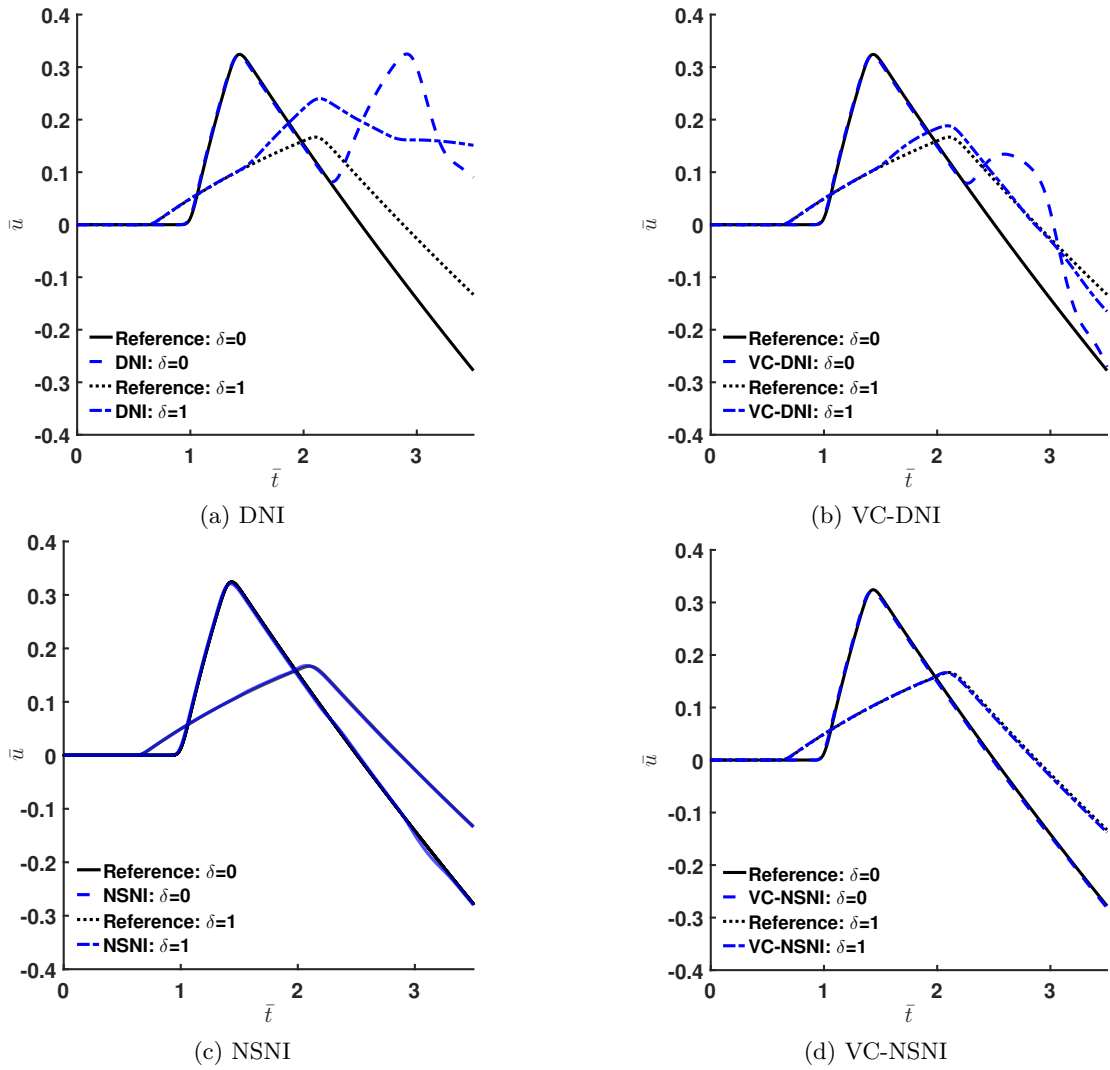


Figure 7: Displacement time histories using the L-S theory with various integration methods.

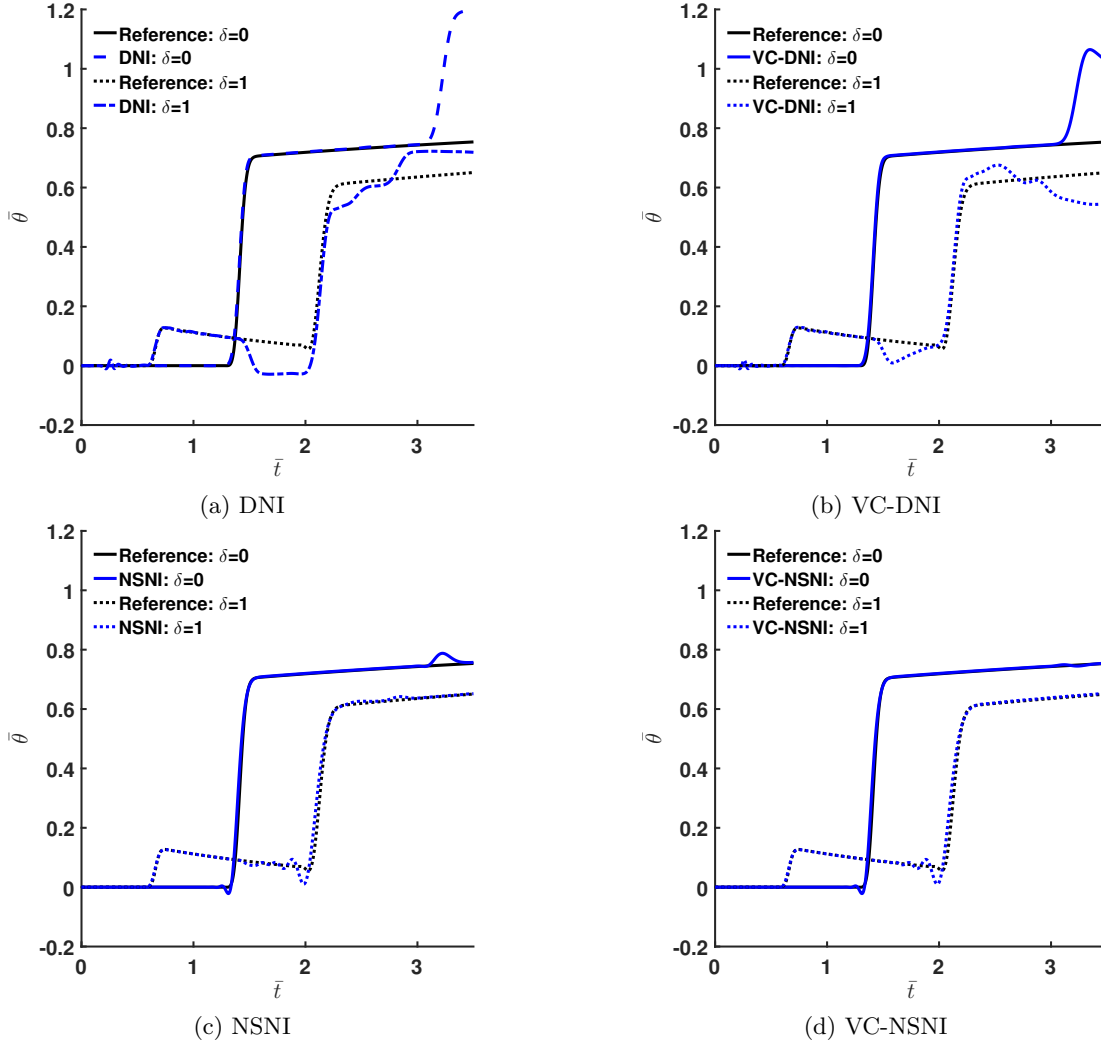


Figure 8: Time histories of temperature change using the L-S theory with various integration methods.

6.1.3 Relaxation time study

In the explicit numerical time integration scheme, the critical time step of the hyperbolic equation is of linear order of the nodal spacing, Δx , or the length of an element in FEM. In contrast, parabolic equations require a time step that is proportional to the square of the nodal spacing, and explicit methods are widely considered to be impractical since spatially refined solutions are always desired for accuracy.

To use a larger time step and obtain solutions close to the classical thermoelasticity theory, we have found that one can select relaxation times in the G-L and L-S theories by setting the thermal wave speed equal to the solid elastic wave speed c_s . Further impetus is provided by the fact that this second sound speed is generally available for most materials, and this also yields a single critical time step for uniformly solving the coupled equations monolithically in time. Here we select the relaxations times

using the following:

$$\begin{aligned}
c_s &= \sqrt{\frac{\lambda + 2\mu}{\rho}} = c_{T,GL} = \sqrt{\frac{k}{t_2 \rho c_p}}, & \rightarrow t_2 &= \frac{k}{(\lambda + 2\mu)c_p}, \\
c_s &= \sqrt{\frac{\lambda + 2\mu}{\rho}} = c_{T,LS} = \sqrt{\frac{k}{t_0 \rho c_p}}, & \rightarrow t_0 &= \frac{k}{(\lambda + 2\mu)c_p}.
\end{aligned} \tag{92}$$

The above selection of relaxation times yields the single critical time step $\Delta t_{cr} = \Delta x/c_s$.

For the problem at hand, the material properties result in the relaxation times $t_2 = 1.05 \times 10^{-12}$ s and $t_0 = 1.05 \times 10^{-12}$ s for the G-L and L-S theories, respectively. For the G-L theory with a second relaxation time t_1 , we set the two relaxation times equal to each other as $t_1 = t_2$. Time histories for classical and generalized thermoelasticity for the displacement and temperature change are shown in Figures 9 and 10. It can be seen from the figures that when the relaxation times are defined using the elastic wave speed, the results are indistinguishable from the classical results for both the coupled and uncoupled cases, and both the G-L and L-S theories. By setting both sound speeds equal, the relaxation times are small enough such that the classical theory is nearly recovered. However here, results close to the classical theory are obtained without a severe time step restriction.

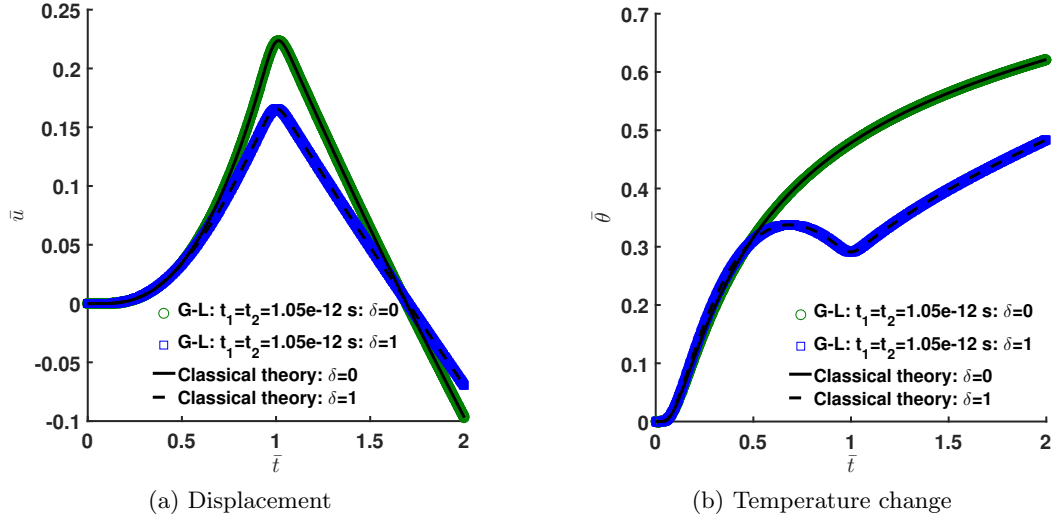


Figure 9: Time histories for the first Danilovskaya problem with the classical theory, and the G-L theory with relaxation times $t_1 = t_2 = 1.05 \times 10^{-12}$ s.

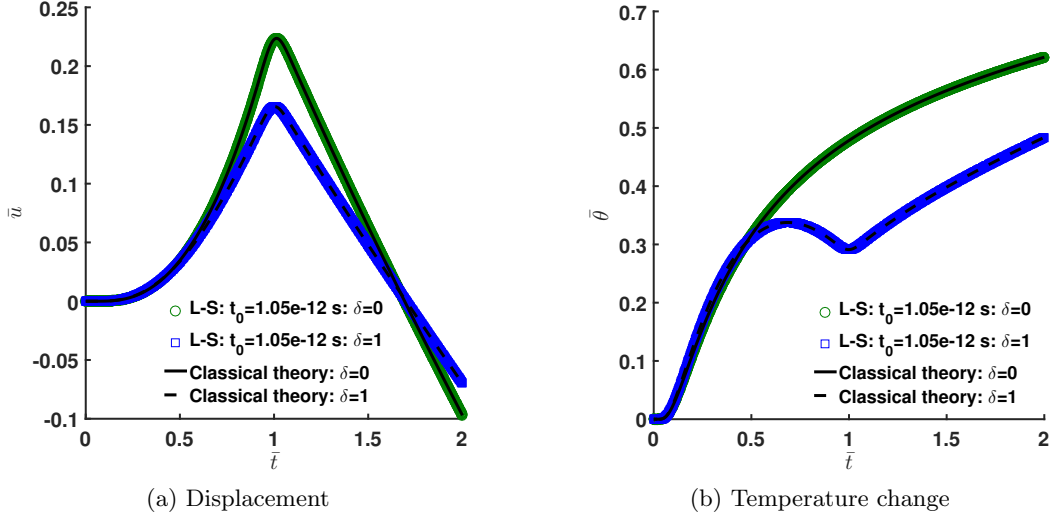


Figure 10: Time histories for the first Danilovskaya problem with the classical theory, and the L-S theory with relaxation time $t_0 = 1.05 \times 10^{-12}$ s.

6.2 Thermoplasticity: necking of an isotropic bar

The necking of an isotropic bar including thermal effects is used as a benchmark for thermoplasticity. For saving computational cost, we use a half bar (with symmetry condition) to perform the simulation. The dimensions of the half-bar shown in Figure 11 are $L_0 = 5.334$ cm, $a_0 = 0.6298$ cm, and $a_1 = 0.6413$ cm.

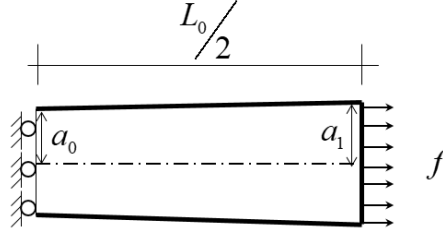


Figure 11: Depiction of tension test with force f and dimensions indicated.

The properties of the bar are density $\rho = 7,800$ kg/m³, Young's modulus $E = 206.9$ GPa, Poisson's ratio $\nu = 0.29$, heat capacity $c_p = 460$ m²/(s²K), thermal conductivity $k = 45$ m · kg/(s³K), thermal expansion coefficient $\alpha = 10^{-5}$ K⁻¹, Taylor-Quinney factor $\chi = 0.9$, initial temperature $T_0 = 293$ K, and the yield stress is

$$K(\bar{e}_p) = \sigma_y^0 + \alpha_y \bar{e}_p + (\sigma_y^\infty - \sigma_y^0)(1 - e^{\beta_1 \bar{e}_p}) \quad (93)$$

where \bar{e}_p is the equivalent plastic strain, $\alpha_y = 0.12924$ GPa, $\sigma_y^0 = 0.45$ GPa, $\sigma_y^\infty = 0.715$ GPa, and $\bar{\beta}_1 = 16.93$.

When the thermal effect is considered, the yield stress can be modified as

$$K(\bar{e}_p, \theta) = \sigma_y^0(\theta) + \alpha_y(\theta) \bar{e}_p + (\sigma_y^\infty(\theta) - \sigma_y^0(\theta))(1 - e^{\beta_1 \bar{e}_p}) \quad (94)$$

where

$$\sigma_y^0(\theta) = \sigma_y^0(1 - \omega_0\theta) \quad (95a)$$

$$\sigma_y^\infty(\theta) = \sigma_y^\infty(1 - \omega_h\theta) \quad (95b)$$

$$\alpha_y(\theta) = \alpha_y(1 - \omega_h\theta) \quad (95c)$$

and here $\omega_0 = 0.002$, and $\omega_h = 0.002$.

Linear basis, a normalized support of 2.0, and a cubic B-spline kernel are used to construct the RK approximation. Figure 12 shows the RKPM discretization with 5,771 nodes. We found for this simulation SNNI suffices for both stability and accuracy, which can likely be attributed to the coarseness and uniformity of the discretization [45, 12]. For non-uniform particles or finer nodal spacing, VC-NSNI should be used as demonstrated in the previous examples.

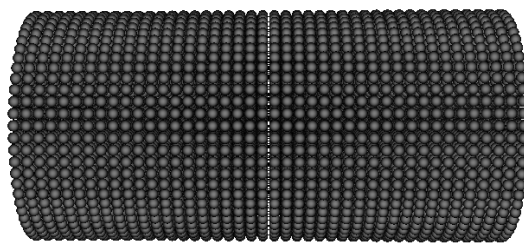


Figure 12: RKPM discretization.

We first consider the classical parabolic energy equation (44). Figure 13 depicts the deformation with the equivalent plastic strain values at 26% elongation. The elongation rate is set to 3 m/s with the time step $\Delta t = 1 \times 10^{-8}$ s. The maximum value of the equivalent plastic strain in this study is close to the numerical results by other methods [27, 46].

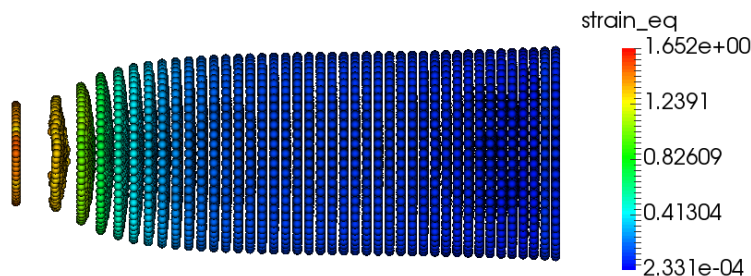


Figure 13: Final elongation with equivalent plastic strain values.

Figure 14 shows the evolution of the radius at the center of the bar and the force-displacement relationship, along with experimental data. It can be seen that RKPM agrees with the reference FEM results (denoted as Seitz et al.) [46], and the experimental data in [42]. For the reduction in radius, RKPM is in better agreement with experimental data than the reference.

For the temperature field, no experimental data is available, so the computational results from [46] are employed as a reference. Figure 15a shows that the thermal

response in the necking region by the proposed nodally integrated RKPM is in agreement with the reference result.

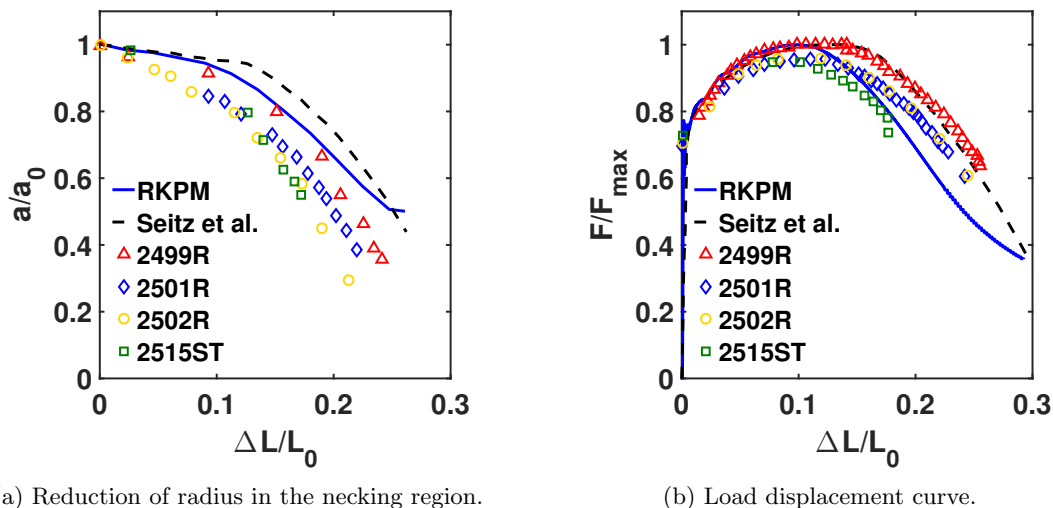


Figure 14: Comparison of RKPM mechanical response in the necking problem with experimental data.

To release the time step restriction of the parabolic equation, we now consider the hyperbolic energy equation (denoted as RKPM-Hyperbolic) with Cattaneo heat conduction (46).

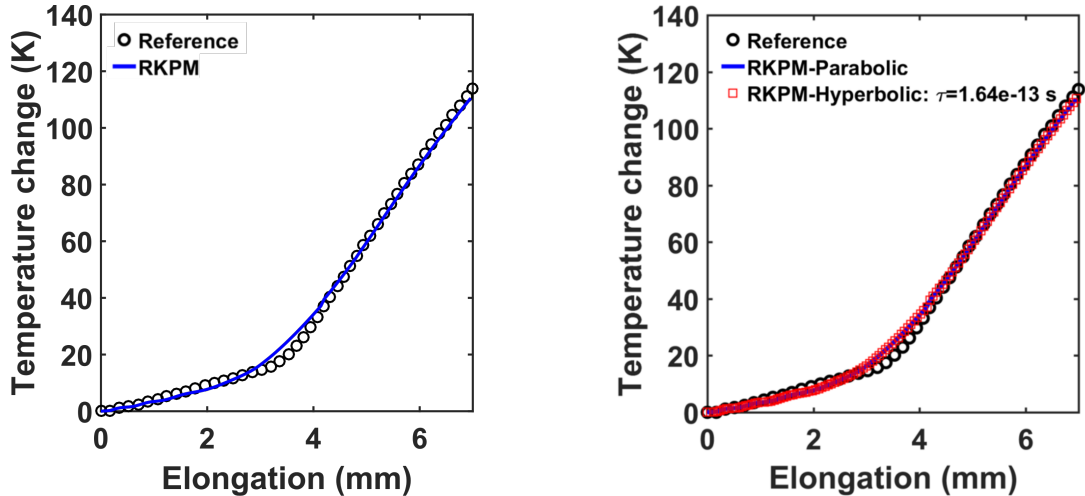
As before, we set the thermal wave speed equal to the elastic wave speed to yield a single critical time step of linear order in the nodal spacing (using linear one-dimensional finite elements as a reference):

$$c_s = \sqrt{E/\rho} = c_{T,C} = \sqrt{k/\tau c_p \rho} \quad \rightarrow \quad \tau = \frac{k}{E c_p} = 4.7282 \times 10^{-13} \text{ s} \quad (96)$$

where $c_{T,C} = \sqrt{k/(\tau \rho c_p)}$ is the wave speed for Cattaneo heat conduction. Thus the critical time step is $\Delta t_{\text{cr}} = \Delta x/c_{T,C} = \Delta x/c_s$. For general considerations, one should consider the p -wave and shear wave velocity for a sharper estimate.

Figure 15b shows the RKPM response using the parabolic and hyperbolic formulations. Both agree with the reference solution, as well as each other. The parabolic and hyperbolic results are virtually indistinguishable.

This example, that uses properties of a real material, seems to indicate that the strategy of setting the thermal sound speed to the solid sound speed is a reasonable approach to achieve explicit analysis with a less restrictive (and uniform) critical time step, meanwhile achieving results similar to the classical theory. In addition, since the data for second sound speeds is not generally available for most materials in typical engineering environments, this is also one way to select the relaxation times for the hyperbolic formulation such that the classical results are achieved for all intents and purposes.



(a) Comparison of RKPM thermal response in the necking problem with results from [46]. (b) Temperatures for the classical theory and the hyperbolic theory equating sound speeds.

Figure 15: Comparisons of RKPM thermal response in the necking problem.

7 Conclusions

In this two-part paper, a stable, accurate, and efficient nodally integrated RKPM approach for thermomechanical problems has been presented. First, the instability in pure nodal quadrature was investigated using thermoelasticity as a model problem. It was shown that this results in node-to-node oscillations typical of nodal integration of meshfree methods in solid mechanics problems, yet the magnitude of the oscillations is several orders of magnitude higher. A naturally stabilized nodal integration (NSNI) was then proposed to stabilize the solution in an efficient manner. This approach of using implicit gradient expansions, has previously been shown to provide accelerated computations, with a 10-20 times CPU speed-up over stress-point type methods. The method was clearly shown to provide stability in both classical and generalized thermoelasticity theories. However, it was also shown that pure NSNI is insufficient for acceptable accuracy in both theories. Therefore, the variational consistency (VC) conditions for n th order exactness and convergence for the two-field problem were derived, and a uniform correction on test function gradients for both fields was adopted. This correction is performed node-by-node with small symmetric systems of equations, and hence increases the computational cost minimally. It should be noted that this approach alone does not provide stability, since it does not address the issue with the trial functions admitting spurious modes. Nevertheless, the combined VC-NSNI method was shown to provide both stability and accuracy in classical and generalized thermoelasticity. These techniques were also shown to be essentially uncoupled, so that no additional issues arise with the implementation of the two combined. These methods were then extended to thermoplasticity. Good agreement with analytical and numerical reference solutions was achieved, as well as agreement with experimental data.

For efficient explicit analysis, hyperbolic theories for both thermoelasticity and

thermoplasticity were investigated. In these models, rather than an infinite propagation of temperature information, a so-called second sound exists, and the use of these theories is well justified from a physical standpoint. Yet, this second sound speed is not well characterized for most engineering materials in most temperature environments. Therefore, equating the second sound speed with the first was investigated. The basis of this approach is the fact that the critical time step for both the equation of motion and generalized thermomechanical models are governed by the nodal spacing and the first and second sound speeds, respectively. While purely a numerical approach for selecting the associated relaxation times in the generalized equations, it was shown that this approach yields results very close to the classical theory since the resulting relation times are extremely small, at least for the problems tested herein. Therefore, since the classical thermomechanical theories are well-accepted in terms of their predictive capabilities, this provides an approach to solve coupled thermomechanical problems without a severe time step restriction.

Now that a stable and effective thermomechanical RKPM has been established, future work will entail applying this method to coupled problems where finite elements encounter great difficulty, e.g., additive manufacturing where topological changes in the domain are present, and subtractive manufacturing such as machining with material failure and separation.

Acknowledgments Both authors greatly acknowledge the support of this work by Penn State, and the endowment of the L. Robert and Mary L. Kimball Early Career Professorship. The first author also acknowledges the support of the Missile Defence Agency through Karagozian and Case Inc. subcontract #PSU 190337.000. Proofing of this manuscript by Jennifer Dougal is also acknowledged and appreciated.

References

- [1] A. E. Abouelregal and A. M. Zenkour. The effect of fractional thermoelasticity on a two-dimensional problem of a mode I crack in a rotating fiber-reinforced thermoelastic medium. *Chinese Physics B*, 22(10):108102, 2013.
- [2] L. Adam and J.-P. Ponthot. Thermomechanical modeling of metals at finite strains: First and mixed order finite elements. *International Journal of Solids and Structures*, 42(21-22):5615–5655, 2005.
- [3] F. Armero and J. C. Simo. A priori stability estimates and unconditionally stable product formula algorithms for nonlinear coupled thermoplasticity. *International Journal of Plasticity*, 9(6):749–782, 1993.
- [4] J. Baek, J. Chen, G. Zhou, K. Arnett, M. Hillman, G. Hegemier, and S. Hardesty. A semi-Lagrangian RKPM with node-based shock algorithm for explosive welding simulation. *Computational Mechanics*, In press.
- [5] A. Bagri, H. Taheri, M. R. Eslami, and S. Fariborz. Generalized coupled thermoelasticity of a layer. *Journal of Thermal Stresses*, 29(4):359–370, 2006.

- [6] K.-J. Bathe. *Finite element procedures*. Klaus-Jurgen Bathe, 2006.
- [7] Y. T. Beni and M. R. Movahhedy. Consistent arbitrary Lagrangian Eulerian formulation for large deformation thermo-mechanical analysis. *Materials & Design*, 31(8):3690–3702, 2010.
- [8] G. T. Camacho and M. Ortiz. Adaptive Lagrangian modelling of ballistic penetration of metallic targets. *Computer methods in applied mechanics and engineering*, 142(3-4):269–301, 1997.
- [9] C. Cattaneo. On a form of the heat equation eliminating the paradox of an instantaneous propagation. *Account. Render*, 247:431–433, 1958.
- [10] J. Chen and G. F. Dargush. Boundary element method for dynamic poroelastic and thermoelastic analyses. *International Journal of Solids and Structures*, 32(15):2257–2278, 1995.
- [11] J.-S. Chen, M. Hillman, and S.-W. Chi. Meshfree Methods: Progress Made after 20 Years. *Journal of Engineering Mechanics*, 2016.
- [12] J.-S. Chen, M. Hillman, and M. Rüter. An arbitrary order variationally consistent integration for Galerkin meshfree methods. *International Journal for Numerical Methods in Engineering*, 95(5):387–418, 2013.
- [13] J.-S. Chen, W. K. Liu, M. Hillman, S. W. Chi, Y. Lian, and M. A. Bessa. Reproducing Kernel Approximation and Discretization. In E. Stein, R. de Borst, and T. J. R. Hughes, editors, *Encyclopedia of Computational Mechanics*. John Wiley & Sons, Ltd., Chichester, 2nd edition, 2017.
- [14] J.-S. Chen, C. Pan, C. Roque, and H.-P. Wang. A lagrangian reproducing kernel particle method for metal forming analysis. *Computational mechanics*, 22(3):289–307, 1998.
- [15] J.-S. Chen, C. Pan, C.-T. Wu, and W. K. Liu. Reproducing Kernel Particle Methods for large deformation analysis of non-linear structures. *Computer Methods in Applied Mechanics and Engineering*, 139(1-4):195–227, 1996.
- [16] J.-S. Chen, C.-T. Wu, S. Yoon, and Y. You. A stabilized conforming nodal integration for galerkin mesh-free methods. *International journal for numerical methods in engineering*, 50(2):435–466, 2001.
- [17] J.-S. Chen and Y. Wu. Stability in lagrangian and semi-lagrangian reproducing kernel discretizations using nodal integration in nonlinear solid mechanics. In *Advances in meshfree techniques*, pages 55–76. Springer, 2007.
- [18] J.-S. Chen, S. Yoon, and C.-T. Wu. Non-linear version of stabilized conforming nodal integration for Galerkin mesh-free methods. *International Journal for Numerical Methods in Engineering*, 53(12):2587–2615, 2002.
- [19] J.-S. Chen, X. Zhang, and T. Belytschko. An implicit gradient model by a reproducing kernel strain regularization in strain localization problems. *Computer Methods in Applied Mechanics and Engineering*, 193(27-29):2827–2844, 2004.

- [20] M. Chester. Second sound in solids. *Physical Review*, 131(5):2013, 1963.
- [21] V. Danilouskaya. Thermal stresses in elastic half space due to sudden heating of its boundary. *Pelageya Yakovlevna Kochina*, 14:316–321, 1950.
- [22] A. C. Eringen. *Mechanics of continua*. Robert E. Krieger Publishing Co., Huntington, New York, 1980.
- [23] Z. Fan and B. Li. Meshfree simulations for additive manufacturing process of metals. *Integrating Materials and Manufacturing Innovation*, 8(2):144–153, 2019.
- [24] A. E. Green and K. A. Lindsay. Thermoelasticity. *Journal of Elasticity*, 2(1):1–7, 1972.
- [25] P.-C. Guan, J.-S. Chen, Y. Wu, H. Teng, J. Gaidos, K. Hofstetter, and M. Al-saleh. Semi-Lagrangian reproducing kernel formulation and application to modeling earth moving operations. *Mechanics of Materials*, 41(6):670–683, 2009.
- [26] P.-C. Guan, S.-W. Chi, J.-S. Chen, T. Slawson, and M. J. Roth. Semi-Lagrangian reproducing kernel particle method for fragment-impact problems. *International Journal of Impact Engineering*, 38(12):1033–1047, 2011.
- [27] M. Hillman and J.-S. Chen. An accelerated, convergent, and stable nodal integration in Galerkin meshfree methods for linear and nonlinear mechanics. *International Journal for Numerical Methods in Engineering*, 107:603–630, 2016.
- [28] M. Hillman, J.-S. Chen, and S.-W. Chi. Stabilized and variationally consistent nodal integration for meshfree modeling of impact problems. *Computational Particle Mechanics*, 1(3):245–256, 2014.
- [29] S. M. Hosseini, J. Sladek, and V. Sladek. Meshless local Petrov–Galerkin method for coupled thermoelasticity analysis of a functionally graded thick hollow cylinder. *Engineering analysis with boundary elements*, 35(6):827–835, 2011.
- [30] P. Hosseini-Tehrani, M. R. Eslami, and S. Azari. Analysis of thermoelastic crack problems using Green–Lindsay Theory. *Journal of Thermal Stresses*, 29(4):317–330, 2006.
- [31] T. J. Hughes. *The finite element method: linear static and dynamic finite element analysis*. Dover Publications, Inc., Mineola, New York, 2012.
- [32] T. J. R. Hughes and J. Winget. Finite rotation effects in numerical integration of rate constitutive equations arising in large deformation analysis. *International Journal for Numerical Methods in Engineering*, 15(12):1862–1867, 1980.
- [33] M. A. Kouchakzadeh and A. Entezari. Analytical solution of classic coupled thermoelasticity problem in a rotating disk. *Journal of Thermal Stresses*, 38(11):1267–1289, 2015.
- [34] B. Li, F. Habbal, and M. Ortiz. Optimal transportation meshfree approximation schemes for fluid and plastic flows. *International journal for numerical methods in engineering*, 83(12):1541–1579, 2010.

- [35] S. Li and W. K. Liu. Synchronized reproducing kernel interpolant via multiple wavelet expansion. *Computational Mechanics*, 21:28–47, 1998.
- [36] S. Li and W. K. Liu. Meshfree and particle methods and their applications. *Appl. Mech. Rev.*, 55(1):1–34, 2002.
- [37] L.-E. Lindgren. Numerical modelling of welding. *Computer Methods in Applied Mechanics and Engineering*, 195(48):6710–6736, 2006.
- [38] W. K. Liu, S. Jun, and Y. F. Zhang. Reproducing kernel particle methods. *International Journal for Numerical Methods in Fluids*, 20(8-9):1081–1106, 1995.
- [39] H. W. Lord and Y. Shulman. A generalized dynamical theory of thermoelasticity. *Journal of the Mechanics and Physics of Solids*, 15(5):299–309, 1967.
- [40] S. H. Mallik and M. Kanoria. A unified generalized thermoelasticity formulation: application to penny-shaped crack analysis. *Journal of Thermal stresses*, 32(9):943–965, 2009.
- [41] T. D. Marusich and M. Ortiz. Modelling and simulation of high-speed machining. *International Journal for Numerical Methods in Engineering*, 38(21):3675–3694, 1995.
- [42] D. M. Norris Jr, B. Moran, J. K. Scudder, and D. F. Quinones. A computer simulation of the tension test. *Journal of the Mechanics and Physics of Solids*, 26(1):1–19, 1978.
- [43] X. Pan, C. T. Wu, W. Hu, and Y. Wu. A momentum-consistent stabilization algorithm for Lagrangian particle methods in the thermo-mechanical friction drilling analysis. *Computational Mechanics*, 64(3):625–644, 2019.
- [44] J.-H. Prevost and D. Tao. Finite element analysis of dynamic coupled thermoelasticity problems with relaxation times. *Journal of applied mechanics*, 50(4a):817–822, 1983.
- [45] M. A. Puso, E. Zywicz, and J. S. Chen. A new stabilized nodal integration approach. *Lecture Notes in Computational Science and Engineering*, 57:207–217, 2007.
- [46] A. Seitz, W. A. Wall, and A. Popp. A computational approach for thermoelasto-plastic frictional contact based on a monolithic formulation using non-smooth nonlinear complementarity functions. *Advanced Modeling and Simulation in Engineering Sciences*, 5(1):5, 2018.
- [47] H. H. Sherief and N. M. El-Maghraby. A mode-I crack problem for an infinite space in generalized thermoelasticity. *Journal of Thermal Stresses*, 28(5):465–484, 2005.
- [48] H. H. Sherief, N. M. El-Maghraby, and A. A. Allam. Stochastic thermal shock problem in generalized thermoelasticity. *Applied Mathematical Modelling*, 37(3):762–775, 2013.

- [49] D. C. Simkins and S. Li. Meshfree simulations of thermo-mechanical ductile fracture. *Computational Mechanics*, 38(3):235–249, 2006.
- [50] J. C. Simo and C. Miehe. Associative coupled thermoplasticity at finite strains: Formulation, numerical analysis and implementation. *Computer Methods in Applied Mechanics and Engineering*, 98(1):41–104, 1992.
- [51] P. H. Tehrani and M. R. Eslami. Boundary element analysis of coupled thermoelasticity with relaxation times in finite domain. *AIAA journal*, 38(3):534–541, 2000.
- [52] P. Vernotte. Les paradoxes de la theorie continue de l’equation de la chaleur. *Comptes rendus*, 246:3154–3155, 1958.
- [53] H. Wang, H. Liao, Z. Fan, J. Fan, L. Stainier, X. Li, and B. Li. The Hot Optimal Transportation Meshfree (HOTM) method for materials under extreme dynamic thermomechanical conditions. *Computer Methods in Applied Mechanics and Engineering*, 364:112958, 2020.
- [54] C. T. Wu, Y. Wu, D. Lyu, X. Pan, and W. Hu. The momentum-consistent smoothed particle Galerkin (MC-SPG) method for simulating the extreme thread forming in the flow drill screw-driving process. *Computational Particle Mechanics*, 7(2):177–191, 2020.
- [55] J. Wu and D. Wang. An accuracy analysis of Galerkin meshfree methods accounting for numerical integration. *Computer Methods in Applied Mechanics and Engineering*, 375:113631, 2021.
- [56] Q. Yang, L. Stainier, and M. Ortiz. A variational formulation of the coupled thermo-mechanical boundary-value problem for general dissipative solids. *Journal of the Mechanics and Physics of Solids*, 54(2):401–424, 2006.
- [57] H. Yousefi, A. T. Kani, and I. M. Kani. Multiscale RBF-based central high resolution schemes for simulation of generalized thermoelasticity problems. *Frontiers of Structural and Civil Engineering*, 13(2):429–455, 2019.
- [58] A. Zamani, R. B. Hetnarski, and M. R. Eslami. Second sound in a cracked layer based on Lord–Shulman theory. *Journal of Thermal Stresses*, 34(3):181–200, 2011.

Appendix A: Small-strain thermoelasticity

With $\eta^p = 0$, the Helmholtz free energy function (6) for thermoelasticity can be written as

$$\phi = e - \theta\eta \tag{97}$$

For small-strain thermoelasticity, the free energy function is a function of strain and the temperature $\phi(\boldsymbol{\varepsilon}, \theta)$ with

$$\dot{\phi}(\boldsymbol{\varepsilon}, \theta) = \frac{\partial \phi}{\partial \boldsymbol{\varepsilon}} \dot{\boldsymbol{\varepsilon}} + \frac{\partial \phi}{\partial \theta} \dot{\theta}. \tag{98}$$

With the assumption (97) and (98), the dissipation inequality (2a) becomes

$$\Omega_{\text{thermech}} = \left(\frac{1}{\rho} \boldsymbol{\sigma} - \frac{\partial \phi}{\partial \boldsymbol{\varepsilon}} \right) : \dot{\boldsymbol{\varepsilon}} + \left(\eta + \frac{\partial \phi}{\partial \theta} \right) \dot{\theta} \geq 0. \quad (99)$$

Which yields the constitutive relations

$$\eta = - \frac{\partial \phi}{\partial \theta} \quad (100)$$

and

$$\boldsymbol{\sigma} = \rho \frac{\partial \phi}{\partial \boldsymbol{\varepsilon}}. \quad (101)$$

Assuming $\boldsymbol{\varepsilon} = \mathbf{0}$ and $\theta = \theta_0$ in the reference state, (101) becomes

$$\boldsymbol{\sigma} = \mathbf{D} : \boldsymbol{\varepsilon} - \boldsymbol{\beta} \theta, \quad \text{or} \quad \boldsymbol{\sigma} = \mathbf{D} : (\boldsymbol{\varepsilon} - \boldsymbol{\alpha} \theta), \quad \text{or} \quad \boldsymbol{\sigma} = 2\mu \text{dev}(\boldsymbol{\varepsilon}) + K \text{tr}(\boldsymbol{\varepsilon}) - 3\alpha(\theta - \theta_0) \mathbf{I} \quad (102)$$

where $\boldsymbol{\alpha}$ contains the thermal expansion coefficients, K is bulk modulus and

$$\mathbf{D} = \rho \frac{\partial^2 \phi}{\partial \boldsymbol{\varepsilon}^2}, \quad (103a)$$

$$\boldsymbol{\beta} = \mathbf{D} : \boldsymbol{\alpha} = -\rho \frac{\partial^2 \phi}{\partial \boldsymbol{\varepsilon} \partial \theta}. \quad (103b)$$

Also, the entropy for small strain can be expressed as

$$\eta(\boldsymbol{\varepsilon}, \theta) = - \frac{\partial \phi}{\partial \theta} = - \frac{\partial \phi}{\partial \theta} \Big|_0 - \frac{\partial^2 \phi}{\partial \boldsymbol{\varepsilon} \partial \theta} \Big|_0 : \boldsymbol{\varepsilon} - \frac{\partial^2 \phi}{\partial \theta^2} \Big|_0 (\theta - \theta_0) \quad (104)$$

where $|_0$ means that the quantity is evaluated at the reference state. With (100), (102), (103), and $(\theta - \theta_0)/\theta \approx (\theta - \theta_0)/\theta_0$, and The specific heat capacity is $c_p = \theta \frac{\partial \eta}{\partial \theta} \approx \theta_0 \frac{\partial \eta}{\partial \theta}$ the entropy (104) can be written as

$$\eta(\boldsymbol{\varepsilon}, \theta) = \eta_0 + \frac{3K\alpha}{\rho} \text{tr}(\boldsymbol{\varepsilon}) + \frac{\theta - \theta_0}{\theta_0} c_p, \quad (105a)$$

$$\dot{\eta}(\boldsymbol{\varepsilon}, \theta) = \frac{3K\alpha}{\rho} \text{tr}(\dot{\boldsymbol{\varepsilon}}) + \frac{\dot{\theta}}{\theta_0} c_p. \quad (105b)$$

Substitution of (105b) and $\boldsymbol{\beta} = 3K\alpha$ into (7) with the Fourier's law (4) yields

$$\rho c_p \frac{\theta}{\theta_0} \dot{\theta} + \theta \boldsymbol{\beta} \text{tr}(\dot{\boldsymbol{\varepsilon}}) = k \nabla \cdot \nabla \theta + Q. \quad (106)$$

With the assumption $\theta \approx \theta_0$, the energy equation becomes

$$\rho c_p \dot{\theta} + \theta_0 \boldsymbol{\beta} \text{tr}(\dot{\boldsymbol{\varepsilon}}) = k \nabla \cdot \nabla \theta + Q \quad (107)$$

which is the same as (12).

Appendix B: Finite-strain thermoplasticity

First, taking time derivative of the Helmholtz free energy function one obtains

$$\dot{\phi} = \dot{e} - \dot{\theta}\eta - \theta\dot{\eta} + \dot{\theta}\eta^p + \theta\dot{\eta}^p. \quad (108)$$

With the assumption (108) and (40), the dissipation inequality (2a) becomes

$$\begin{aligned} \Omega_{\text{thermech}} = \rho(\mathbf{P} - \frac{\partial\phi^e}{\partial\mathbf{F}^e}\frac{\mathbf{F}^e}{\mathbf{F}}) : \dot{\mathbf{F}} + (-(\eta - \eta^p) + \rho\frac{\partial\phi}{\partial\theta})\dot{\theta} + \\ \rho\frac{\partial\phi^e}{\partial\mathbf{F}^e}\frac{\mathbf{F}^e}{\mathbf{F}^p} : \dot{\mathbf{F}}^p + \rho\frac{\partial\phi^p}{\partial v}\dot{v} + \theta\dot{\eta}^p \geq 0. \end{aligned} \quad (109)$$

where $\mathbf{F} = \mathbf{F}^e\mathbf{F}^p$; \mathbf{F}^e is the deformation gradient; \mathbf{F}^e and \mathbf{F}^p are the elastic and plastic part of the deformation gradient, respectively. Since \mathbf{F} , $\dot{\mathbf{F}}$, θ , and $\dot{\theta}$ are arbitrary values, we obtain the constitutive relations of

$$\mathbf{P} = \frac{\partial\phi}{\partial\mathbf{F}^e}\frac{\partial\mathbf{F}^e}{\partial\mathbf{F}}, \quad \eta - \eta^p = \rho\frac{\partial\phi}{\partial\theta} \quad (110)$$

where \mathbf{P} is the first Piola-Kirchhoff stress.

Here we define (109) into two parts

$$\mathbf{D}_{\text{mech}} = \rho\frac{\partial\phi^e}{\partial\mathbf{F}^e}\frac{\mathbf{F}^e}{\mathbf{F}^p} : \dot{\mathbf{F}}^p + \rho\frac{\partial\phi^p}{\partial v}\dot{v} = \boldsymbol{\Sigma} : \mathbf{D}^p + \rho\frac{\partial\phi^p}{\partial v}\dot{v}, \quad (111a)$$

$$\mathbf{D}_{\text{ther}} = \theta\dot{\eta}^p \quad (111b)$$

where $\boldsymbol{\Sigma} = 2\mathbf{C}^e\frac{\partial\phi^e}{\partial\mathbf{C}^e}$ is the Mandel stress tensor; $\mathbf{C} = \mathbf{F}^T\mathbf{F}$ denotes the right Cauchy-Green tensor and \mathbf{C}^e is the elastic part, and $\mathbf{D}^p = \text{sym}(\dot{\mathbf{F}}^p\mathbf{F}^{p-1})$ is the symmetric part of the plastic velocity gradient. Substitution (108), (42), and (111) into (7) with the Fourier's law (4) yields

$$\rho c_p \dot{\theta} = k\nabla \cdot \nabla\theta + Q + \mathbf{D}_{\text{mech}} + \theta\frac{\partial(\mathbf{P} : \dot{\mathbf{F}} - \mathbf{D}_{\text{mech}})}{\partial\theta} \quad (112)$$

where the last term is the elasto-plastic heating.

The simplification can be written with a dissipation factor χ and $\mathbf{D}_{\text{mech}} - \theta\frac{\partial\mathbf{D}_{\text{mech}}}{\partial\theta}$ is replaced to a total plastic power \dot{w}^p as following

$$\rho c_p \dot{\theta} = k\nabla \cdot \nabla\theta + Q + \theta\frac{\partial(\mathbf{P} : \dot{\mathbf{F}})}{\partial\theta} + \chi\dot{w}^p. \quad (113)$$

In applications of metal thermoplasticity, the plastic dissipation is much greater than thermoelastic heating. Therefore, we rewrite the energy equation neglecting the thermoelastic heating

$$\rho c_p \dot{\theta} = k\nabla \cdot \nabla\theta + Q + \chi\dot{w}^p$$

which is (43).